Nonlinear Subsynchronous Oscillation Damping Controller for Direct-Drive Wind Farms With VSC-HVDC Systems

Shao, Bingbing; Zhao, Shuqiang; Yang, Y.; Gao, Benfeng; Wang, Liyuan; Blaabjerg, F.

Published in:
IEEE Journal of Emerging and Selected Topics in Power Electronics

DOI (link to publication from Publisher):
10.1109/JESTPE.2020.3025081

Publication date:
2022

Document Version
Accepted author manuscript, peer reviewed version

Nonlinear Sub-synchronous Oscillation Damping Controller for Direct-drive Wind Farms with VSC-HVDC Systems

Bingbing Shao, *Student Member, IEEE*, Shuqiang Zhao, Yongheng Yang, *Senior Member, IEEE*, Benfeng Gao, Liyuan Wang, and Frede Blaabjerg, *Fellow, IEEE*

***Abstract*—Due to the sub-synchronous interaction between the grid-side converter (GSC) of wind farms and the rectifier (REC) of voltage source converter-based high voltage direct current (VSC-HVDC) transmission system, sub-synchronous oscillations (SSOs) may occur in direct-drive wind farms with VSC-HVDC systems. Considering the nonlinearities and uncertainties of the system, a nonlinear SSO mitigation strategy is proposed in this paper based on the feedback linearization theory and sliding mode control (SMC). The feedback linearization theory is used to eliminate the nonlinearities, and the SMC is adopted to improve the robustness against uncertainties and disturbances. The proposed feedback linearization sliding mode control (FLSMC) takes the advantages of feedback linearization control (FLC) and SMC. The FLC transforms the nonlinear forms of the GSC and REC into the linear forms through the coordinate transformation and feedback. Considering that the FLC is sensitive to parameter uncertainties and external disturbances, the SMC is combined with the FLC to improve the system robustness. An eigenvalue analysis and time-domain simulations are carried out, which demonstrates that the FLC outperforms over the traditional proportional-integral control for the SSO mitigation and decoupling. Meanwhile, the FLSMC shows better robustness against parameter uncertainties and external disturbances over the FLC and traditional damping control.**

***Index Terms*—direct-drive wind farm, feedback linearization, sliding mode control (SMC), sub-synchronous oscillation (SSO), voltage source converter-based high voltage direct current (VSC-HVDC).**

NOMENCLATURE

DFIG	Doubly fed induction generator.
PMSG	Permanent magnet synchronous generator.
WTG	Wind turbine generator.
VSC-HVDC	Voltage source converter-based high voltage direct current.
DDWFV	Direct-drive wind farms with the VSC-HVDC.
SSO	Sub-synchronous oscillation.
FACTS	Flexible ac transmission systems.
REC	Rectifier.
SSDC	Sub-synchronous damping control.
PI	Proportional-integral.
EFL	Exact feedback linearization.
PFL	Partial feedback linearization.
FLC	Feedback linearization control.
PV	Photovoltaic.
GSC	Grid-side converter.
MSC	Machine-side converter.
PLL	Phase-locked loop.
FLSMC	Feedback linearization sliding mode control.
SMC	Sliding mode control.
u_{DC}	DC voltage of the GSC.
C	DC capacitor of the back-back converter.
i_{dc1}	DC-side input current of the wind farm.
i_{gd}, i_{gq}	d- and q-axis output current of the GSC.
u_{wd}, u_{wq}	d- and q-axis output voltage of the GSC.
L_g	Filter inductance of the wind farm.
u_{gd}, u_{gq}	d- and q-axis primary-side voltage of the transformer T_1.
ω_g	Angular line frequency.
R_c, L_c	Equivalent resistance and inductance of the phase reactor.
C_f	Filter capacitor of the VSC-HVDC.
u_{sd}, u_{sq}	d- and q-axis voltage across C_f.
i_{2d}, i_{2q}	d- and q-axis input current of the VSC-HVDC.
i_{sd}, i_{sq}	d- and q-axis current flowing to the phase reactor.
u_{vd}, u_{vq}	d- and q-axis output voltage of the REC.
C_{dc}	DC capacitor of the VSC-HVDC.
u_{dc1}	DC voltage across C_{dc}.
i_{dc}	DC-side input current of the VSC-HVDC.
u_{dc}	Equivalent DC voltage source of the inverter station.
ω_0	Reference angular frequency.
n_w	Order of the GSC.
u_{w1}, u_{w2}	Control input variables of the GSC.
$h_{w1}(x)$, $h_{w2}(x)$	Control output variables of the GSC.

This work was supported in part by the Natural Science Foundation of Hebei Province under Grant E2017502075, in part by the Fundamental Research Funds for the Central Universities of China under Grant 2018ZD001, and in part by the Joint Postgraduate Training Program of North China Electric Power University.

B. Shao, S. Zhao, B. Gao, and L. Wang are with the Key Laboratory of Distributed Energy Storage and Microgrid of Hebei Province (North China Electric Power University), Baoding 071003, Hebei Province, China (e-mail: shaobingbing1223@163.com; zsqdl@163.com; gaobenfeng@126.com; liyuanwang96@163.com).

Y. Yang and F. Blaabjerg are with the Department of Energy Technology, Aalborg University, Aalborg 9220, Denmark (e-mail: yoy@et.aau.dk; fbl@et.aau.dk).

n_v	Order of the REC.
u_{v1}, u_{v2}	Control input variables of the REC.
$h_{v1}(x)$, $h_{v2}(x)$	Control output variables of the REC.
r_w	Total relative degree of the GSC.
r_v	Total relative degree of the REC.
$\boldsymbol{z}_w$, $\boldsymbol{z}_v$	Transformed state variables of the GSC and REC.
$\boldsymbol{\phi}_w$, $\boldsymbol{\phi}_v$	Function of $\boldsymbol{x}_w$, function of $\boldsymbol{x}_v$.
$\boldsymbol{z}_{wo}$, $\boldsymbol{z}_{vo}$	External states to the order of the relative degrees from the GSC and REC.
$\boldsymbol{z}_{wi}$, $\boldsymbol{z}_{vi}$	Internal states associated to the order of $n_w - r_w$ and n_v - r_v.
$\boldsymbol{A}_w$, $\boldsymbol{B}_w$, $\boldsymbol{v}_w$	State matrix, input matrix, and control input of the partially linearized GSC.
$\boldsymbol{A}_v$, $\boldsymbol{B}_v$, $\boldsymbol{v}_v$	State matrix, input matrix, and control input of the partially linearized REC.
v_{w1}, v_{w2}	Pre-control variables of the GSC.
v_{v1}, v_{v2}	Pre-control variables of the REC.
k_{wp1}, k_{wi1}	PI parameters of the DC voltage controller in the GSC.
k_{wp2}, k_{wi2}	PI parameters of the *q*-axis current controller in the GSC.
k_{vp1}, k_{vi1}	PI parameters of the *d*-axis voltage controller in the REC.
k_{vp2}, k_{vi2}	PI parameters of the *q*-axis voltage controller in the REC.
S_{wd}, S_{wq}	*d*- and *q*-axis sliding mode surfaces of the GSC.
ε_{wd}, ε_{wq}	Parameters of constant rate reaching laws in the GSC.
S_{vd}, S_{vq}	*d*- and *q*-axis sliding mode surfaces of the REC.
ε_{vd}, ε_{vq}	Parameters of constant rate reaching laws in the REC.
ref	Subscript indicates the reference of variables.
$\boldsymbol{H}_w$, $\boldsymbol{H}_v$	Uncertainties or disturbances in the GSC and REC.
FLC-GSC	FLC is used in the GSC and the PI control is adopted in the REC.
FLC-REC	FLC is used in the REC and the PI control is adopted in the GSC.
PCC	Point of common coupling.
i_{SSDC}	Output signal of SSDC.
G	Gain of the SSDC.
$(sT_{11}+1)/(sT_{12}+1)$	Phase-lead loop of the SSDC.
$(sT_{21}+1)/(sT_{22}+1)$	Phase-lag loop of the SSDC.
m	Number of phase-lead loops.
n	Number of phase-lag loops.
P_0	Switching loss of the REC.
i_{dc3}	Output current of the REC.

I. Introduction

By 2019, the global installed capacity of the wind power exceeded 651 GW [1]. For the wind energy integration, the DFIG with partial-scale converters and the PMSG with full-scale converters are two popular WTGs [2]. Compared with the DFIG, the PMSG is more efficient and maintenance-free due to the absence of slip rings, brushes, and gearboxes [3]. Meanwhile, with the increase of the capacity and connection distance of offshore wind farms, the VSC-HVDC transmission technology has become an economically feasible solution [4]. Thus, the DDWFV is a promising wind energy integration solution.

However, the stability of offshore wind farms with VSC-HVDC systems is a key issue due to no direct connection from the AC collection bus to a strong AC grid [5]. For instance, as reported in [6], an SSO frequency of about 21 Hz was observed in a wind farm with a VSC-HVDC system. It was found in [5]-[12] that the SSO in wind farms with VSC-HVDC systems was mainly related to the interaction between the controllers of wind farms and the REC controller of the VSC-HVDC. With the impedance analysis methods in [5]-[7], the SSO in the DDWFV was arguably originated by the interaction between the wind farm inverter controller and the VSC-HVDC REC controller. The controller parameters affect the SSO stability to a large extent. Meanwhile, the impedance analysis method was also used to analyze the stability of the DFIG-based wind farms with VSC-HVDC systems [8]. It has been found in [8] that the rotor-side converter controller of the DFIG and the REC controller of the VSC-HVDC play an important role in the SSO stability. With the eigenvalue analysis methods in [9]-[11], it has been revealed that the DDWFV experiences dynamic SSO instability due to the interactions between different controllers of the wind farm and the REC station. Moreover, in [12], an open-loop modal method was used, which has indicated that when the PMSGs participate in the open-loop modal couplings, strong sub-synchronous interactions between the converter control of the VSC-HVDC and the PMSGs cause the SSOs. The SSO can damage system equipment [13], [14], reduce the output power [15]-[18], and degrade the power quality [19], [20]. Therefore, it is of importance to develop an efficient SSO damping control strategy for the DDWFV.

At present, there are three types of methods to mitigate the SSO in wind farms: 1) using FACTS [21]-[26], 2) adding SSO damping to the converter controllers of wind farms [6], [27]-[32], and 3) optimizing the parameters of the present converter controllers [10], [33], [34]. However, using FACTS devices to mitigate the SSO in wind farms is not economically feasible. In addition, the SSDC is designed based on the approximately linearized model of a system. This implies that the controller lacks robustness and can achieve acceptable performance only within a predefined range of uncertainties. The disadvantage also exists in the methods by optimizing the controller parameters. Although this issue can be addressed by adaptively adjusting the parameters [35], [36], the dynamics are slow, and PI controller parameters exceeding a certain range weakens the wind farms' faults ride-through capacity [27], [37]. Moreover, the major focus has been put on the SSO mitigation in wind farms connected to series-compensated system or a weak AC grid [38], whereas few studies are carried out to mitigate the SSO of wind farms with VSC-HVDC systems [6], [32], [34]. In [6], [32], the arm virtual resistance method, resonant voltage compensation method, and harmonic circulating current suppression were discussed to mitigate the SSO of the DDWFV. Meanwhile, optimizing the controller parameters of the DDWFV can improve the SSO [34]. As the SSO mitigation methods in [6], [32], [34] were designed based

This article has been accepted for publication in a future issue of this journal, but has not been fully edited. Content may change prior to final publication. Citation information: DOI 10.1109/JESTPE.2020.3025081, IEEE Journal of Emerging and Selected Topics in Power Electronics

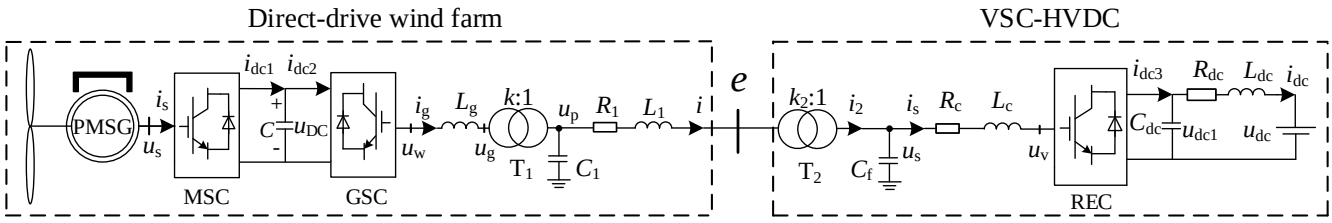

Fig. 1. System diagram of direct-drive wind farms interfaced with VSC-HVDC systems (MSC - machine-side converter, GSC - grid-side converter, REC - rectifier), where R_1, L_1, and C_1 are the resistance, inductance, and capacitance of the collector line, respectively. R_{dc}, L_{dc}, and C_{dc} are the DC-side resistance, inductance, and capacitance of the VSC-HVDC, respectively.

on the approximately linearized model of the DDWFV, the inherent nonlinearities of the DDWFV cannot be considered, and then acceptable performance is only achieved within a predefined set of operations. To overcome this, a robust damping controller should be proposed to mitigate the SSO of the DDWFV over a wide range of operating conditions.

The main idea behind FLC is the reconfiguration of the nonlinear system using a transformation and feedback loop in order to obtain a linear relationship between the input and output of the system [39]. As the FLC can eliminate the nonlinearities of the DDWFV without additional devices, using the FLC to mitigate the SSO can fill in the above gaps. The FLC has been successfully used in other cases, e.g., in PV systems for decoupling the dynamical models of multiple PV units [40], in PMSG wind power systems for low-voltage ride-through operation [41], in HVDC systems for decoupling power and circulating currents [42], and in DC microgrids for maintaining the desired voltage at the common dc bus [43]. However, the FLC was rarely used to suppress the SSO, and the application of the FLC in the DDWFV has not been explored. In [44], [45], the SSO in series-compensated DFIG-based wind farms was identified, and a nonlinear damping controller using the feedback linearization technique was designed to mitigate the SSO. Different from the case in [44], [45], the FLC is proposed in this paper to mitigate the SSO of the DDWFV. Although the FLC design process of the GSC is nearly the same as that in [44], [45], the PFL and internal dynamics of the REC are examined in this paper, which will be discussed in Section III. Additionally, considering that the FLC lacks intrinsic robustness against parametric uncertainties and external disturbances [46], a FLSMC scheme integrating FLC and SMC is proposed in this paper. The SMC stands out because of its inherent characteristics such as robustness, insensitivity to system variation, and simple implementation [47]. On one hand, the SMC relieves the dependence of the FLC on the accurate mathematical model. On the other hand, the FLC helps to establish a linear sliding mode function, and then the system dynamic performance is improved [48]. The main contributions of this paper are summarized as follows:

- The partial feedback linearization of the DDWFV is achieved, and the effectiveness and superiority of the FLC compared to the PI control in SSO mitigation are verified under various operating conditions.
- The FLSMC is designed to improve the robustness of the FLC, and the stability and robustness of the FLSMC are verified by theoretical analysis. Meanwhile, the superiority of the FLSMC compared to the PI, FLC, and SSDC is demonstrated.

The rest of this paper is organized as follows. In Section II, the model of the DDWFV is developed. In Section III, the FLC is designed through four steps. In Section IV, the SMC is combined with the FLC to improve the robustness of the DDWFV. The structures, SSO mitigation performances, and robustness of the PI, FLC, and FLSMC are discussed in Section V. The SSO mitigation performances, decoupling characteristics and robustness of the proposed controller are then evaluated in Section VI through an eigenvalue analysis and time-domain simulations. Concluding remarks are given in Section VII.

II. Modeling of the DDWFV

The diagram of the DDWFV is divided into the direct-drive wind farm and the VSC-HVDC, as shown in Fig. 1. 40 wind turbines with the power rating of 5 MW for each are lumped into one unit of 200 MW capacity. Then, an equivalent model of a PMSG with the 200-MW installed capacity is equivalent to a direct-drive wind farm. The system parameters of the DDWFV are shown in Appendix A. It was indicated in [5] that the SSO of the DDWFV resulted from the interaction between the GSC and REC. Therefore, the control objectives of the proposed damping controller should be the GSC and REC. The dynamic mathematical models of the GSC and REC are derived in the following:

A. Dynamic Models of the GSC and REC

$$\begin{cases} \dfrac{\mathrm{d}u_{\mathrm{DC}}}{\mathrm{d}t} = \dfrac{i_{\mathrm{dc1}}}{C} - \dfrac{3i_{gd}u_{wd}}{2Cu_{\mathrm{DC}}} - \dfrac{3i_{gq}u_{wq}}{2Cu_{\mathrm{DC}}} \\ \dfrac{\mathrm{d}i_{gd}}{\mathrm{d}t} = -\dfrac{1}{L_{\mathrm{g}}}u_{gd} + \omega_{\mathrm{g}}i_{gq} + \dfrac{1}{L_{\mathrm{g}}}u_{wd} \\ \dfrac{\mathrm{d}i_{gq}}{\mathrm{d}t} = -\dfrac{1}{L_{\mathrm{g}}}u_{gq} - \omega_{\mathrm{g}}i_{gd} + \dfrac{1}{L_{\mathrm{g}}}u_{wq} \end{cases} \tag{1}$$

$$\begin{cases} \dfrac{\mathrm{d}u_{sd}}{\mathrm{d}t} = \dfrac{1}{C_{\mathrm{f}}}i_{2d} - \dfrac{1}{C_{\mathrm{f}}}i_{sd} + \omega_{\mathrm{g}}u_{sq} \\ \dfrac{\mathrm{d}u_{sq}}{\mathrm{d}t} = \dfrac{1}{C_{\mathrm{f}}}i_{2q} - \dfrac{1}{C_{\mathrm{f}}}i_{sq} - \omega_{\mathrm{g}}u_{sd} \\ \dfrac{\mathrm{d}i_{sd}}{\mathrm{d}t} = \dfrac{1}{L_{\mathrm{c}}}u_{sd} - \dfrac{R_{\mathrm{c}}}{L_{\mathrm{c}}}i_{sd} - \dfrac{1}{L_{\mathrm{c}}}u_{vd} + \omega_{\mathrm{g}}i_{sq} \\ \dfrac{\mathrm{d}i_{sq}}{\mathrm{d}t} = \dfrac{1}{L_{\mathrm{c}}}u_{sq} - \dfrac{R_{\mathrm{c}}}{L_{\mathrm{c}}}i_{sq} - \dfrac{1}{L_{\mathrm{c}}}u_{vq} - \omega_{\mathrm{g}}i_{sd} \\ \dfrac{\mathrm{d}u_{\mathrm{dc1}}}{\mathrm{d}t} = \dfrac{3u_{vd}i_{sd}}{2C_{\mathrm{dc}}u_{\mathrm{dc1}}} + \dfrac{3u_{vq}i_{sq}}{2C_{\mathrm{dc}}u_{\mathrm{dc1}}} - \dfrac{i_{\mathrm{dc}}}{C_{\mathrm{dc}}} \end{cases} \tag{2}$$

This article has been accepted for publication in a future issue of this journal, but has not been fully edited. Content may change prior to final publication. Citation information: DOI 10.1109/JESTPE.2020.3025081, IEEE Journal of Emerging and Selected Topics in Power Electronics

According to Fig. 1, the dynamics of the GSC are shown in (1), where the state variables are u_{dc}, i_{gd}, and i_{gq}, and the control input variables are u_{wd} and u_{wq}.

Furthermore, referring to Fig. 1, the dynamics of the REC are represented by (2), where the state variables are u_{sd}, u_{sq}, i_{sd}, i_{sq}, and u_{dc1}, and the control input variables are u_{vd} and u_{vq}.

B. PI Control Structures of the DDWFV

In the wind farm, the MSC controls the *d*-axis current to be 0, which minimizes the loss of the generator. The DC voltage and reactive power are controlled by the GSC. The *d*-*q* rotating coordinate system is set based on the node voltage u_p, and the *q*-axis component of u_p is the input of a PLL. The control structures of the MSC, GSC, and PLL are shown in Figs. 2-4.

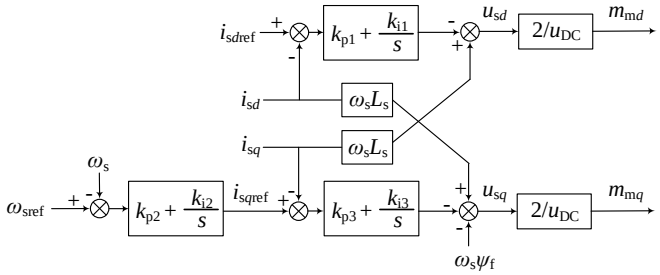

Fig. 2. Control structure of the machine-side converter with PI controllers, where m_{md} and m_{mq} are the *d*- and *q*-axis modulation signals; ω_s is the electric speed of the PMSG; ψ_f represents the magnetic flux.

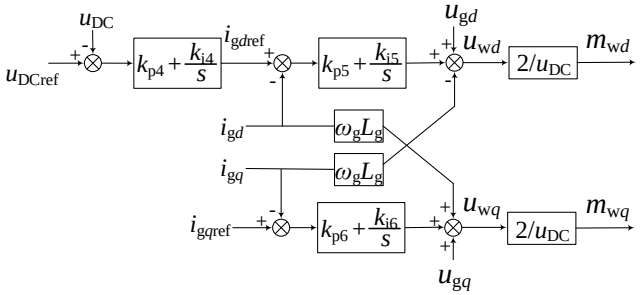

Fig. 3. Control structure of the grid-side converter with PI controllers, where m_{wd} and m_{wq} are the *d*- and *q*-axis modulation signals.

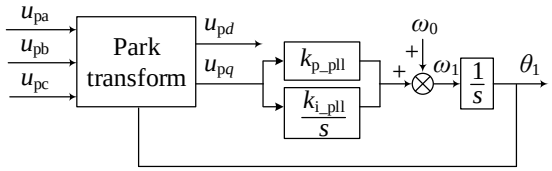

Fig. 4. Control structure of the phase-locked loop in the wind farm, where k_{p_pll} and k_{i_pll} are the proportional and integral coefficients.

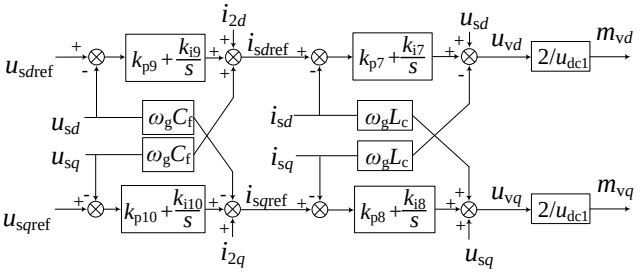

Fig. 5. Control structure of the rectifier with PI controllers, where m_{vd} and m_{vq} are the *d*- and *q*-axis modulation signals.

In the VSC-HVDC, the REC controls the AC voltage amplitude and frequency, and the inverter controls the DC voltage. Supposing that the onshore AC grid is strong, the DC bus voltage can be kept constant by the inverter station. Then, a constant DC voltage source is equivalent to the inverter station, which is shown as u_{dc} in Fig. 1. Notably, the PLL of the VSC-HVDC takes the reference angular frequency ω_0 as an input signal, and $\omega_0 = 2\pi f_0$ ($f_0 = 50$ Hz) [5]. The control structure of the REC is shown in Fig. 5.

III. FLC OF THE DDWFV

Traditional PI control strategies are designed based on the specific operating point of the DDWFV. The performance of the strategies is easily affected by the nonlinearities of the DDWFV. Therefore, the FLC is applied in the GSC and REC to cancel the nonlinearities. The design of the FLC mainly includes four steps: 1) scrutinizing EFL or PFL, 2) transforming the nonlinear system to a linear system by the coordinate transformation and feedback, 3) if the PFL is performed, the initial system should be divided into external dynamics and internal dynamics. The external dynamics need to be designed properly, and the stability of internal dynamics needs to be ensured, 4) deriving the control law, and the pre-control variables after coordinate transformation are designed. Each step is discussed in detail as follows.

A. Scrutinizing Feedback Linearization

The first step of designing the FLC is to scrutinize the feedback linearization of the studied systems (1) and (2). Based on the control input $\boldsymbol{u}$ and control output $\boldsymbol{y}$, the dynamic models of (1) and (2) are represented in the general form of multiple-input and multiple-output (MIMO) systems as

$$\begin{cases} \dot{\boldsymbol{x}}_w = \boldsymbol{f}_w(\boldsymbol{x}) + \boldsymbol{g}_{w1}(\boldsymbol{x})u_{w1} + \boldsymbol{g}_{w2}(\boldsymbol{x})u_{w2} \\ \boldsymbol{y}_w = \boldsymbol{h}_w(\boldsymbol{x}) \end{cases} \tag{3}$$

$$\begin{cases} \dot{\boldsymbol{x}}_v = \boldsymbol{f}_v(\boldsymbol{x}) + \boldsymbol{g}_{v1}(\boldsymbol{x})u_{v1} + \boldsymbol{g}_{v2}(\boldsymbol{x})u_{v2} \\ \boldsymbol{y}_v = \boldsymbol{h}_v(\boldsymbol{x}) \end{cases} \tag{4}$$

in which (3) represents the affine nonlinear system of the GSC, $\boldsymbol{x}_w = [u_{DC}, i_{gd}, i_{gq}]^T$, $n_w = 3$, $u_{w1} = u_{wd}$ and $u_{w2} = u_{wq}$, $\boldsymbol{h}_w(x) = [h_{w1}(x), h_{w2}(x)]^T = [u_{DC}, i_{gq}]^T$. (4) represents the affine nonlinear system of the REC. $\boldsymbol{x}_v = [u_{sd}, u_{sq}, i_{sd}, i_{sq}, u_{dc1}]^T$, $n_v = 5$, $u_{v1} = u_{vd}$ and $u_{v2} = u_{vq}$, $\boldsymbol{h}_v(x) = [h_{v1}(x), h_{v2}(x)]^T = [u_{sd}, u_{sq}]^T$. The expressions of $\boldsymbol{f}_w(x)$, $\boldsymbol{g}_w(x)$, $\boldsymbol{f}_v(x)$, and $\boldsymbol{g}_v(x)$ are shown in Appendix B.

The total relative degree determines the feedback linearizability of a nonlinear system. The system should be exactly linearized if the total relative degree equals to the order of the system, or the system can be partially linearized if the total relative degree is less than the order of the system. The total relative degree of the GSC is calculated as [42]

$$\begin{cases} L_{g_{w1}} L_{f_w}^{1-1} h_{w1}(\boldsymbol{x}) = -3i_{gd} / 2Cu_{DC} \\ L_{g_{w2}} L_{f_w}^{1-1} h_{w1}(\boldsymbol{x}) = -3i_{gq} / 2Cu_{DC} \\ L_{g_{w1}} L_{f_w}^{1-1} h_{w2}(\boldsymbol{x}) = 0 \\ L_{g_{w2}} L_{f_w}^{1-1} h_{w2}(\boldsymbol{x}) = 1/L_g \end{cases} \tag{5}$$

where L defines the Lie derivative with respect to the corresponding subscripts. For example, $L_f^{r_i-1} h_i(x)$ represents the $(r_i - 1)$th Lie derivative of $h_i(x)$ along $f(x)$, where r_i is the relative

This article has been accepted for publication in a future issue of this journal, but has not been fully edited. Content may change prior to final publication. Citation information: DOI 10.1109/JESTPE.2020.3025081, IEEE Journal of Emerging and Selected Topics in Power Electronics

degree corresponding to the output function $h_i(x)$. As $\boldsymbol{B}$ = [-3i_{gd}/2Cu_{DC} -3i_{gq}/2Cu_{DC}; 0 1/L_g] is nonsingular, the total relative degree of the GSC is r_w = 1+1 = 2, which is less than the order of the GSC (n_w). Thus, the GSC is partially linearizable. In addition, the total relative degree (r_v) of the REC is calculated to be 4 in the same way. As $r_v < n_v$, the REC is also partially linearizable.

B. Nonlinear Coordinate Transformation and Feedback

Since the GSC and REC can be partial-feedback linearized, the transformed state variables of the GSC and REC, $\boldsymbol{z}_w$ and $\boldsymbol{z}_v$, are written as

$$\boldsymbol{z}_{\mathrm{w}} = \boldsymbol{\phi}_{\mathrm{w}}(\boldsymbol{x}) = [\boldsymbol{z}_{\mathbf{wo}} \quad \boldsymbol{z}_{\mathbf{wi}}]^{\mathrm{T}} \tag{6}$$

$$\boldsymbol{z}_{\mathrm{v}} = \boldsymbol{\phi}_{\mathrm{v}}(\boldsymbol{x}) = [\boldsymbol{z}_{\mathbf{vo}} \quad \boldsymbol{z}_{\mathbf{vi}}]^{\mathrm{T}} \tag{7}$$

Therefore, the partially linearized GSC and REC are expressed as

$$\dot{\boldsymbol{z}}_{\mathrm{wo}} = \boldsymbol{A}_{\mathrm{w}}(\boldsymbol{x})\boldsymbol{z}_{\mathrm{wo}} + \boldsymbol{B}_{\mathrm{w}}(\boldsymbol{x})\boldsymbol{v}_{\mathrm{w}} \tag{8}$$

$$\dot{\boldsymbol{z}}_{\mathrm{vo}} = \boldsymbol{A}_{\mathrm{v}}(\boldsymbol{x})\boldsymbol{z}_{\mathrm{vo}} + \boldsymbol{B}_{\mathrm{v}}(\boldsymbol{x})\boldsymbol{v}_{\mathrm{v}} \tag{9}$$

As the GSC controls the DC voltage and *q*-axis current, and REC controls the *d*- and *q*-axis AC voltage, we have

$$\begin{cases} \boldsymbol{z}_{\mathrm{wo}} = [z_{\mathrm{wo1}} \ z_{\mathrm{wo2}}]^{\mathrm{T}} \\ z_{\mathrm{wo1}} = \phi_{\mathrm{w1}}(\boldsymbol{x}) = h_{\mathrm{w1}}(\boldsymbol{x}) = u_{\mathrm{DC}},\ z_{\mathrm{wo2}} = \phi_{\mathrm{w2}}(\boldsymbol{x}) = h_{\mathrm{w2}}(\boldsymbol{x}) = i_{gq} \end{cases} \tag{10}$$

$$\begin{cases} \boldsymbol{z}_{\mathrm{vo}} = [z_{\mathrm{vo1}} \ z_{\mathrm{vo2}} \ z_{\mathrm{vo3}} \ z_{\mathrm{vo4}}]^{\mathrm{T}} \\ z_{\mathrm{vo1}} = \phi_{\mathrm{v1}}(\boldsymbol{x}) = h_{\mathrm{v1}}(\boldsymbol{x}) = u_{sd} \\ z_{\mathrm{vo2}} = \phi_{\mathrm{v2}}(\boldsymbol{x}) = h_{\mathrm{v2}}(\boldsymbol{x}) = u_{sq} \\ z_{\mathrm{vo3}} = \phi_{\mathrm{v3}}(\boldsymbol{x}) = L_{f_{\mathrm{v}}} h_{\mathrm{v1}}(\boldsymbol{x}) = \dot{u}_{sd} \\ z_{\mathrm{vo4}} = \phi_{\mathrm{v4}}(\boldsymbol{x}) = L_{f_{\mathrm{v}}} h_{\mathrm{v2}}(\boldsymbol{x}) = \dot{u}_{sq} \end{cases} \tag{11}$$

Referring to (1), (2), it gives that

$$\begin{cases} \dot{z}_{\mathrm{wo1}} = \dot{h}_{\mathrm{w1}}(\boldsymbol{x}) = \dfrac{i_{\mathrm{dc1}}}{C} - \dfrac{3i_{gd}}{2Cu_{\mathrm{DC}}}u_{wd} - \dfrac{3i_{gq}}{2Cu_{\mathrm{DC}}}u_{wq} \\ \dot{z}_{\mathrm{wo2}} = \dot{h}_{\mathrm{w2}}(\boldsymbol{x}) = -\dfrac{1}{L_{\mathrm{g}}}u_{gq} - \omega_{\mathrm{g}} i_{gq} + \dfrac{1}{L_{\mathrm{g}}}u_{wq} \end{cases} \tag{12}$$

$$\begin{cases} \dot{z}_{\mathrm{vo1}} = \dot{h}_{\mathrm{v1}}(\boldsymbol{x}) = \dfrac{1}{C_{\mathrm{f}}} i_{2d} - \dfrac{1}{C_{\mathrm{f}}} i_{sd} + \omega_{\mathrm{g}} u_{sq} \\ \dot{z}_{\mathrm{vo2}} = \dot{h}_{\mathrm{v2}}(\boldsymbol{x}) = \dfrac{1}{C_{\mathrm{f}}} i_{2q} - \dfrac{1}{C_{\mathrm{f}}} i_{sq} - \omega_{\mathrm{g}} u_{sd} \\ \dot{z}_{\mathrm{vo3}} = \ddot{h}_{\mathrm{v1}}(\boldsymbol{x}) = \dfrac{\omega_{\mathrm{g}}}{C_{\mathrm{f}}} i_{2q} + \dfrac{R_{\mathrm{c}}}{L_{\mathrm{c}}C_{\mathrm{f}}} i_{sd} - \dfrac{2\omega_{\mathrm{g}}}{C_{\mathrm{f}}} i_{sq} - \\ \dfrac{\omega_{\mathrm{g}}^2 L_{\mathrm{c}}C_{\mathrm{f}} + 1}{L_{\mathrm{c}}C_{\mathrm{f}}} u_{sd} + \dfrac{1}{L_{\mathrm{c}}C_{\mathrm{f}}} u_{vd} \\ \dot{z}_{\mathrm{vo4}} = \ddot{h}_{\mathrm{v2}}(\boldsymbol{x}) = -\dfrac{\omega_{\mathrm{g}}}{C_{\mathrm{f}}} i_{2d} + \dfrac{2\omega_{\mathrm{g}}}{C_{\mathrm{f}}} i_{sd} + \dfrac{R_{\mathrm{c}}}{L_{\mathrm{c}}C_{\mathrm{f}}} i_{sq} - \\ \dfrac{\omega_{\mathrm{g}}^2 L_{\mathrm{c}}C_{\mathrm{f}} + 1}{L_{\mathrm{c}}C_{\mathrm{f}}} u_{sq} + \dfrac{1}{L_{\mathrm{c}}C_{\mathrm{f}}} u_{vq} \end{cases} \tag{13}$$

Applying the linear control technique as $dz_{w01}/dt = v_{w1}$, $dz_{wo2}/dt = v_{w2}$, $dz_{w03}/dt = v_{v1}$, and $dz_{vo4}/dt = v_{v2}$, the nonlinear state feedbacks are obtained as

$$\begin{cases} v_{\mathrm{w1}} = \dfrac{i_{\mathrm{dc1}}}{C} - \dfrac{3i_{gd}}{2Cu_{\mathrm{DC}}}u_{wd} - \dfrac{3i_{gq}}{2Cu_{\mathrm{DC}}}u_{wq} \\ v_{\mathrm{w2}} = -\dfrac{1}{L_{\mathrm{g}}}u_{gq} - \omega_{\mathrm{g}} i_{gq} + \dfrac{1}{L_{\mathrm{g}}}u_{wq} \end{cases} \tag{14}$$

$$\begin{cases} v_{\mathrm{v1}} = \dfrac{\omega_{\mathrm{g}} i_{2q}}{C_{\mathrm{f}}} + \dfrac{R_{\mathrm{c}} i_{sd}}{L_{\mathrm{c}}C_{\mathrm{f}}} - \dfrac{2\omega_{\mathrm{g}} i_{sq}}{C_{\mathrm{f}}} - \dfrac{\omega_{\mathrm{g}}^2 L_{\mathrm{c}}C_{\mathrm{f}} + 1}{L_{\mathrm{c}}C_{\mathrm{f}}} u_{sd} + \dfrac{1}{L_{\mathrm{c}}C_{\mathrm{f}}} u_{vd} \\ v_{\mathrm{v2}} = -\dfrac{\omega_{\mathrm{g}} i_{2d}}{C_{\mathrm{f}}} + \dfrac{2\omega_{\mathrm{g}} i_{sd}}{C_{\mathrm{f}}} + \dfrac{R_{\mathrm{c}} i_{sq}}{L_{\mathrm{c}}C_{\mathrm{f}}} - \dfrac{\omega_{\mathrm{g}}^2 L_{\mathrm{c}}C_{\mathrm{f}} + 1}{L_{\mathrm{c}}C_{\mathrm{f}}} u_{sq} + \dfrac{1}{L_{\mathrm{c}}C_{\mathrm{f}}} u_{vq} \end{cases} \tag{15}$$

where v_{w1}, v_{w2}, v_{v1}, and v_{v2} can be obtained by applying a standard PI control method [41], [42]. The physical control laws of the GSC and REC can be computed from (14) and (15) followed by examining the stability of internal dynamics.

It can be seen from the above analysis that the FLC transforms the original nonlinear systems (1), (2) to the linear systems (8), (9) by coordinate transformations (10), (11) and nonlinear state feedbacks (14), (15).

C. Internal Dynamics Stability

Before deriving the control laws from (14), (15), the internal dynamics stability of the GSC and REC needs to be ensured. The internal dynamics stability of the GSC and REC is guaranteed using the zero-dynamic theory [39], which is shown in Appendix C.

D. Deriving Control Laws

From (14), (15), the FLC control laws of the GSC and REC are obtained as

$$\begin{cases} m_{wd1} = \dfrac{2}{u_{\mathrm{DC}}}u_{wd} = \dfrac{2}{u_{\mathrm{DC}}}\left(\dfrac{2i_{\mathrm{dc1}}u_{\mathrm{DC}} - 3i_{gq}u_{gq}}{3i_{gd}} - \omega_{\mathrm{g}} L_{\mathrm{g}} i_{gq}\right. \\ \left. - \dfrac{2Cu_{\mathrm{DC}}}{3i_{gd}}v_{\mathrm{w1}} - \dfrac{L_{\mathrm{g}} i_{gq}}{i_{gd}}v_{\mathrm{w2}}\right) \\ m_{wq1} = \dfrac{2}{u_{\mathrm{DC}}}u_{wq} = \dfrac{2}{u_{\mathrm{DC}}}(u_{gq} + \omega_{\mathrm{g}} L_{\mathrm{g}} i_{gd} + L_{\mathrm{g}} v_{\mathrm{w2}}) \end{cases} \tag{16}$$

$$\begin{cases} m_{vd1} = \dfrac{2}{u_{\mathrm{dc1}}}u_{vd} = \dfrac{2}{u_{\mathrm{dc1}}}(-\omega_{\mathrm{g}} L_{\mathrm{c}} i_{2q} - R_{\mathrm{c}} i_{sd} + 2\omega_{\mathrm{g}} L_{\mathrm{c}} i_{sq} \\ +(\omega_{\mathrm{g}}^2 L_{\mathrm{c}}C_{\mathrm{f}} + 1)u_{sd} + L_{\mathrm{c}}C_{\mathrm{f}} v_{\mathrm{v1}}) \\ m_{vq1} = \dfrac{2}{u_{\mathrm{dc1}}}u_{vq} = \dfrac{2}{u_{\mathrm{dc1}}}(\omega_{\mathrm{g}} L_{\mathrm{c}} i_{2d} - 2\omega_{\mathrm{g}} L_{\mathrm{c}} i_{sd} - R_{\mathrm{c}} i_{sq} \\ +(\omega_{\mathrm{g}}^2 L_{\mathrm{c}}C_{\mathrm{f}} + 1)u_{sq} + L_{\mathrm{c}}C_{\mathrm{f}} v_{\mathrm{v2}}) \end{cases} \tag{17}$$

from which, it is known that only the pre-control variables (v_{w1}, v_{w2}, v_{v1}, v_{v2}) are not determined. The pre-control variables are normally designed from the following linear control equations [41], [42]:

$$\begin{cases} v_{\mathrm{w1}} = k_{\mathrm{wp1}}(u_{\mathrm{DCref}} - u_{\mathrm{DC}}) + k_{\mathrm{wi1}}\int_0^t (u_{\mathrm{DCref}} - u_{\mathrm{DC}})\mathrm{d}t \\ v_{\mathrm{w2}} = k_{\mathrm{wp2}}(i_{gq\mathrm{ref}} - i_{gq}) + k_{\mathrm{wi2}}\int_0^t (i_{gq\mathrm{ref}} - i_{gq})\mathrm{d}t \end{cases} \tag{18}$$

$$\begin{cases} v_{\mathrm{v1}} = k_{\mathrm{vp1}}(u_{sd\mathrm{ref}} - u_{sd}) + k_{\mathrm{vi1}}\int_0^t (u_{sd\mathrm{ref}} - u_{sd})\mathrm{d}t \\ v_{\mathrm{v2}} = k_{\mathrm{vp2}}(u_{sq\mathrm{ref}} - u_{sq}) + k_{\mathrm{vi2}}\int_0^t (u_{sq\mathrm{ref}} - u_{sq})\mathrm{d}t \end{cases} \tag{19}$$

Accordingly, the control structures of the GSC and REC

This article has been accepted for publication in a future issue of this journal, but has not been fully edited. Content may change prior to final publication. Citation information: DOI 10.1109/JESTPE.2020.3025081, IEEE Journal of Emerging and Selected Topics in Power Electronics

under the FLC are shown in Figs. 6 and 7. As it can be seen from Figs. 3 and 6, Figs. 5 and 7, compared with the PI control, the FLC increases the algebraic computation, but certain *d*- and *q*-axis PI control loops are cancelled, thus reducing the difficulty of PI parameters tuning.

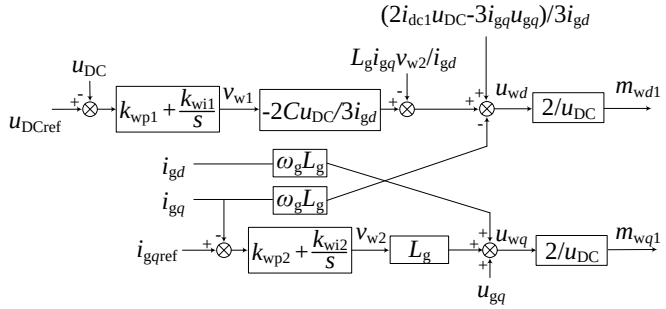

Fig. 6. Control structure of the grid-side converter under the feedback linearization control.

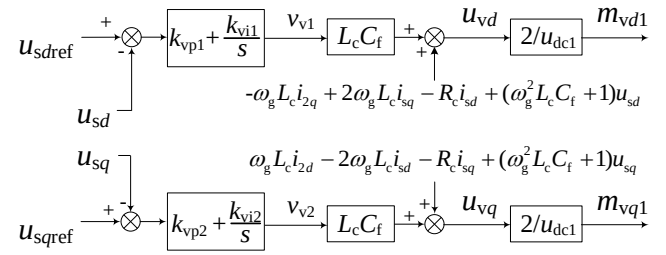

Fig. 7. Control structure of the rectifier under the feedback linearization control.

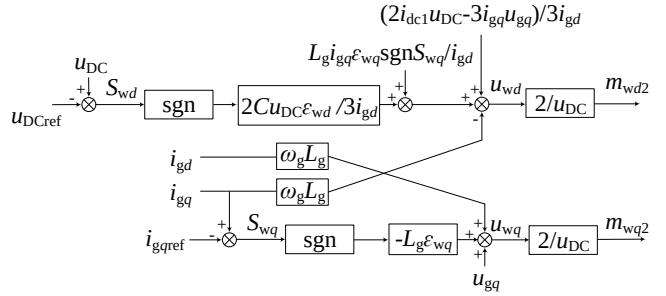

Fig. 8. Control structure of the grid-side converter under the feedback linearization sliding mode control.

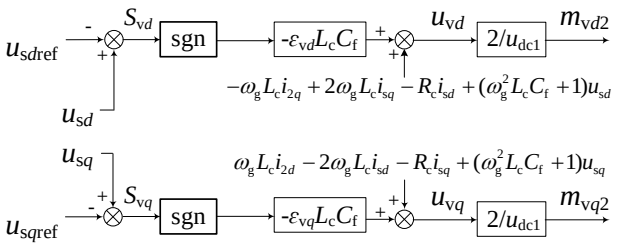

Fig. 9. Control structure of the rectifier under the feedback linearization sliding mode control.

IV. FLSMC OF THE DDWFV

As the FLC is a model-based method, it is sensitive to parameter uncertainties and external disturbances [39]. In order to improve the robustness of the FLC, the SMC is used to design the pre-control variables (v_{w1}, v_{w2}, v_{v1}, v_{v2}) of (16), (17). The SMC offers good properties, such as fast dynamics and insensitivity to external disturbances. The design of SMC mainly includes two steps: 1) designing sliding mode surfaces and 2) deriving equivalent control laws. Then, the stability and robustness of the SMC should be examined.

A. Designing Sliding Mode Surfaces

Since the control objectives of the GSC are DC voltage and *q*-axis current, the sliding mode surface of the GSC is selected as

$$S_{wd}=u_{DC}-u_{DCref},\ S_{wq}=i_{gq}-i_{gqref} \tag{20}$$

Notably, chattering is a major drawback of the SMC, which can be weakened by the rational design of SMC laws [47]. To reduce the system chattering, the SMC law of the GSC is designed based on constant rate reaching law as

$$\begin{cases}\dot{S}_{wd}=-\varepsilon_{wd}\mathrm{sgn}S_{wd}\\ \dot{S}_{wq}=-\varepsilon_{wq}\mathrm{sgn}S_{wq}\end{cases}\quad \varepsilon_{wd},\ \varepsilon_{wq}>0 \tag{21}$$

Smaller ε_{wd} and ε_{wq} imply smaller chattering but longer settling time [49]. Similarly, the SMC law of the REC is designed as

$$\begin{cases}\dot{S}_{vd}=-\varepsilon_{vd}\mathrm{sgn}S_{vd}\\ \dot{S}_{vq}=-\varepsilon_{vq}\mathrm{sgn}S_{vq}\end{cases}\quad \varepsilon_{vd},\ \varepsilon_{vq}>0 \tag{22}$$

where $S_{vd}=u_{sd}-u_{sdref}$, $S_{vq}=u_{sq}-u_{sqref}$.

B. Equivalent Control Laws

From (21), (22), the pre-control variables in (16) and (17) are designed based on the SMC as

$$v_{w1}=-\varepsilon_{wd}\mathrm{sgn}S_{wd},\ v_{w2}=-\varepsilon_{wq}\mathrm{sgn}S_{wq} \tag{23}$$

$$v_{v1}=-\varepsilon_{vd}\mathrm{sgn}S_{vd},\ v_{v2}=-\varepsilon_{vq}\mathrm{sgn}S_{vq} \tag{24}$$

Combining FLC and SMC by substituting (23), (24) into (16), (17), we have the equivalent control laws of the FLSMC as

$$\begin{cases}m_{wd2}=\dfrac{2}{u_{DC}}\Big(\dfrac{2i_{dc1}u_{DC}-3i_{gq}u_{gq}}{3i_{gd}}-\omega_gL_gi_{gq}+\\ \dfrac{2Cu_{DC}}{3i_{gd}}\varepsilon_{wd}\mathrm{sgn}S_{wd}+\dfrac{L_gi_{gq}}{i_{gd}}\varepsilon_{wq}\mathrm{sgn}S_{wq}\Big)\\ m_{wq2}=\dfrac{2}{u_{DC}}(u_{gq}+\omega_gL_gi_{gd}-L_g\varepsilon_{wq}\mathrm{sgn}S_{wq})\end{cases} \tag{25}$$

$$\begin{cases}m_{vd2}=\dfrac{2}{u_{dc1}}(-\omega_gL_ci_{2q}-R_ci_{sd}+2\omega_gL_ci_{sq}+\\ (\omega_g^2L_cC_f+1)u_{sd}-L_cC_f\varepsilon_{vd}\mathrm{sgn}S_{vd})\\ m_{vq2}=\dfrac{2}{u_{dc1}}(\omega_gL_ci_{2d}-2\omega_gL_ci_{sd}-R_ci_{sq}+\\ (\omega_g^2L_cC_f+1)u_{sq}-L_cC_f\varepsilon_{vq}\mathrm{sgn}S_{vq})\end{cases} \tag{26}$$

From (25), (26), the control structures of the GSC and REC under the FLSMC are shown in Figs. 8 and 9.

C. Proof of the Stability and Robustness

$$\begin{cases}V_w(S)=\boldsymbol{S}_w^{\mathrm{T}}\boldsymbol{S}_w=\dfrac{1}{2}S_{wd}^2+\dfrac{1}{2}S_{wq}^2\\ V_v(S)=\boldsymbol{S}_v^{\mathrm{T}}\boldsymbol{S}_v=\dfrac{1}{2}S_{vd}^2+\dfrac{1}{2}S_{vq}^2\end{cases} \tag{27}$$

1) Proof of the Stability: The first objective of the SMC is to

This article has been accepted for publication in a future issue of this journal, but has not been fully edited. Content may change prior to final publication. Citation information: DOI 10.1109/JESTPE.2020.3025081, IEEE Journal of Emerging and Selected Topics in Power Electronics

ensure the convergence of the operating points. To examine the stability, a Lyapunov function is introduced in (27), where $\boldsymbol{S}_{\mathrm{w}} = [S_{wd}\ S_{wq}]^{\mathrm{T}}$, $\boldsymbol{S}_{\mathrm{v}} = [S_{vd}\ S_{vq}]^{\mathrm{T}}$. The SMC is considered asymptotically stable if $\mathrm{d}V_{\mathrm{w}}/\mathrm{d}t < 0$ and $\mathrm{d}V_{\mathrm{v}}/\mathrm{d}t < 0$. The derivative of V_{w} is calculated as

$$\begin{aligned}\dot{V}_{\mathrm{w}}(S) &= \frac{\delta V_{\mathrm{w}}(S)}{\delta S_{\mathrm{wd}}}\frac{\delta S_{\mathrm{wd}}}{\delta t} + \frac{\delta V_{\mathrm{w}}(S)}{\delta S_{wq}}\frac{\delta S_{wq}}{\delta t} = S_{wd}\dot{S}_{wd} + S_{wq}\dot{S}_{wq} \\ &= -\varepsilon_{wd}S_{wd}\mathrm{sgn}S_{wd} - \varepsilon_{wq}S_{wq}\,\mathrm{sgn}\,S_{wq} = -\varepsilon_{wd}\left|S_{wd}\right| - \varepsilon_{wq}\left|S_{wq}\right|\end{aligned} \tag{28}$$

As ε_{wd}, $\varepsilon_{wq} > 0$, $\mathrm{d}V_{\mathrm{w}}/\mathrm{d}t$ is a negative-definite function. Similarly, $\mathrm{d}V_{\mathrm{v}}/\mathrm{d}t$ is also a negative-definite function. Therefore, S_{wd}, S_{wq}, S_{vd}, and S_{vq} approach zero asymptotically, and the proposed FLSMC is asymptotically stable.

2) Proof of the Robustness: Under practical application conditions, parameter uncertainties and external disturbances may appear in the control system. In such conditions, (21) and (22) are rewritten as

$$\dot{\boldsymbol{S}}_{\mathrm{w}} = \boldsymbol{F}_{\mathrm{w}} + \boldsymbol{H}_{\mathrm{w}} \tag{29}$$

$$\dot{\boldsymbol{S}}_{\mathrm{v}} = \boldsymbol{F}_{\mathrm{v}} + \boldsymbol{H}_{\mathrm{v}} \tag{30}$$

where $\boldsymbol{F}_{\mathrm{w}} = [-\varepsilon_{wd}\mathrm{sgn}S_{wd}\ -\varepsilon_{wq}\mathrm{sgn}S_{wq}]^{\mathrm{T}}$, $\boldsymbol{H}_{\mathrm{w}}$ represents the uncertainties or disturbances in the GSC, and $\boldsymbol{H}_{\mathrm{w}} = [H_{wd}\ H_{wq}]^{\mathrm{T}}$; $\boldsymbol{F}_{\mathrm{v}} = [-\varepsilon_{vd}\mathrm{sgn}S_{vd}\ -\varepsilon_{vq}\mathrm{sgn}S_{vq}]^{\mathrm{T}}$, $\boldsymbol{H}_{\mathrm{v}}$ represents the uncertainties or disturbances in the REC, and $\boldsymbol{H}_{\mathrm{v}} = [H_{vd}\ H_{vq}]^{\mathrm{T}}$. Substituting (29) into (28) leads to

$$\begin{aligned}\dot{V}_{\mathrm{w}}(S) &= S_{wd}(-\varepsilon_{wd}\mathrm{sgn}S_{wd} + H_{wd}) + S_{wq}(-\varepsilon_{wq}\,\mathrm{sgn}\,S_{wq} + H_{wq}) \\ &= (-\varepsilon_{wd}\left|S_{wd}\right| + H_{wd}S_{wd}) + (-\varepsilon_{wq}\left|S_{wq}\right| + H_{wq}S_{wq})\end{aligned} \tag{31}$$

According to the Lyapunov's stability theorem, the GSC under the FLSMC features strong robustness if (31) is less than 0. Thus, the coefficients of the SMC should be designed properly as

$$\varepsilon_{wd} > H_{wd} \text{ and } \varepsilon_{wq} > H_{wq} \tag{32}$$

Similarly, to assure the robustness of the REC under the FLSMC, ε_{vd} and ε_{vd} need to be designed larger than H_{vd} and H_{vq}, respectively. Considering that the coefficients of the FLSMC affect the chattering, settling time, and robustness, they should be designed to make a trade-off among these performances.

V. Comparison Among PI, FLC, and FLSMC

In this section, the structures, SSO mitigation performances, and robustness of the PI, FLC, and FLSMC are compared, as shown in Table I. From the perspective of control structures under different control strategies (see Figs. 3, 5, 6-9), the PI control strategy has the most PI loops (3 in the GSC and 4 in the REC), but the algebraic computation is light. In contrast, the number of PI loops in both the GSC and REC under the FLC are two, whereas the algebraic computation is moderate. It is worth pointing out that the FLSMC has no PI loops, and its algebraic computation is almost at the same level as the FLC. From the perspective of SSO mitigation performances, as the PI control strategy is designed based on the approximately linearized model of the DDWFV, it can only achieve desired performance within certain operation conditions. Thus, compared with the FLC and FLSMC, the PI control strategy performs poorly in SSO mitigation under various operating conditions. From the perspective of robustness under different control strategies, as the SMC improves the robustness of the DDWFV, the FLSMC shows stronger robustness than the PI control and FLC. In brief, the FLSMC provides an acceptable trade-off among complexity, SSO damping performances, and robustness.

TABLE I
Structures, SSO Mitigation Performances and Robustness of Different Control Strategies.

Control strategies	Number of PI controllers	Algebraic computation	SSO mitigation performances	Robustness
PI	7	Low	Low	Weak
FLC	4	Moderate	High	Weak
FLSMC	0	Moderate	High	Strong

It is worth mentioning that the heuristic algorithms (e.g., genetic algorithm, simulated annealing algorithm, and particle swarm algorithm) can also be used to mitigate the SSO of series-compensated DFIG-based wind farms by optimizing controller parameters [25], [50]-[52]. In the optimization with heuristic algorithms, the objective function was set based on the small-signal model of a system, and the robustness was improved based on the transfer function from disturbances to control output [52]. Compared with the FLC and FLSMC, the optimization method does not need to examine the feedback linearization and internal dynamics of a system. However, as the objective functions in [25], [50]-[52] are the linearized state-space model, the method cannot achieve a satisfactory performance over a wide range of operating conditions. This implies that the heuristic algorithms may face the risk of local optima [51]. Although this issue can be solved by performing the optimization every time when the operating point changes, the process is time-consuming. In [51], [52], representative operating conditions were included in the optimization process, and then controller parameters were optimized to make compromises among different conditions. However, it is difficult to cover the full range of operating conditions in the optimization process, and a high amount of calculation is required.

VI. Controller Performance Evaluation

In this section, the SSO mitigation performances and step response characteristics of the PI and FLC are first compared. Then, the robustness of the FLC and FLSMC is benchmarked. Finally, the performance of FLSMC is compared with a SSDC to verify its superiority. The well-tuned control parameters of the PI, FLC, FLSMC, and SSDC are shown in Appendix D.

A. Evaluation of SSO Mitigation Performance

The SSO mitigation performances of the PI and FLC are compared through eigenvalue analysis and PSCAD/EMTDC simulations under different wind speeds, DC voltages and sizes of the wind farm.

1) Different Wind Speeds: Define FLC-GSC as the scenario that the FLC is used in the GSC and the PI control is used in the REC; Define FLC-REC as the scenario that the FLC is used in the REC and the PI control is used in the GSC. Based on the small-signal model of Fig. 1 [9], the root locus of the SSO modes under different wind speeds is shown in Fig. 10 (every two adjacent points have a wind speed difference of 0.5 m/s).

This article has been accepted for publication in a future issue of this journal, but has not been fully edited. Content may change prior to final publication. Citation information: DOI 10.1109/JESTPE.2020.3025081, IEEE Journal of Emerging and Selected Topics in Power Electronics

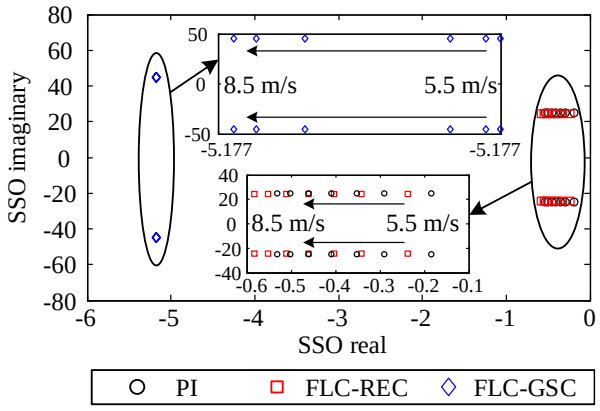

Fig. 10. Root locus of the SSO mode under different wind speeds.

It can be seen from Fig. 10 that the FLC-GSC significantly improves the SSO damping under different wind speeds. However, compared with the PI control, the SSO damping under the FLC-REC does not increase obviously. The main reason is that the GSC participates more in the SSO mode compared with the REC. The normalized participation factors of the SSO mode under the PI control are shown in Fig. 11, where $x_4 = \int(u_{DC} - u_{DCref})dt$, $x_5 = \int(i_{gdref} - i_{gd})dt$, and $x_7 = \int(i_{sdref} - i_{sd})dt$. It can be seen from Fig. 11 that the state variables of the GSC participate more in the SSO mode than those of the REC. Thus, it is better to use the FLC in the GSC.

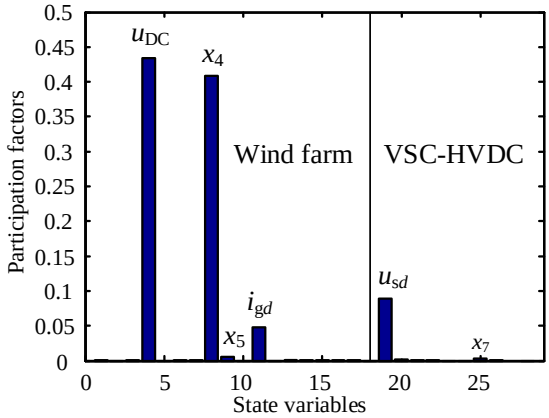

Fig. 11. Normalized participation factors of the SSO mode.

To verify the theoretical analysis in Fig. 10, simulations are performed when a three-phase short-circuit ground fault happens in the common bus (point *e* in Fig. 1) at 2 s and is cleared after 50 ms. The responses of the wind farm DC voltage and PCC voltage are shown in Fig. 12. It can be seen from Fig. 12(a) that the DC voltage exhibits decayed SSO under the PI, FLC-GSC, and FLC-REC. The SSO frequency under the PI control at 8 m/s wind speed is 1/0.189 (5.291) Hz. As the state variables of the REC participate in the SSO with less participation factors under the PI control (see Fig. 11), replacing PI control with FLC in the REC almost has no effect on the SSO mitigation. Thus, the DC voltage responses under the FLC-REC and PI control are nearly unchanged, as shown in Fig. 12(a). Compared with the FLC-REC, as the state variables of the GSC participate in the SSO with more participation factors under the PI control (see Fig. 11), replacing PI control with the FLC in the GSC will affect the SSO mitigation to a large extent. Thus, the DC voltage under the FLC-GSC decays faster and the fluctuation is smaller, as shown in Fig. 12(a).

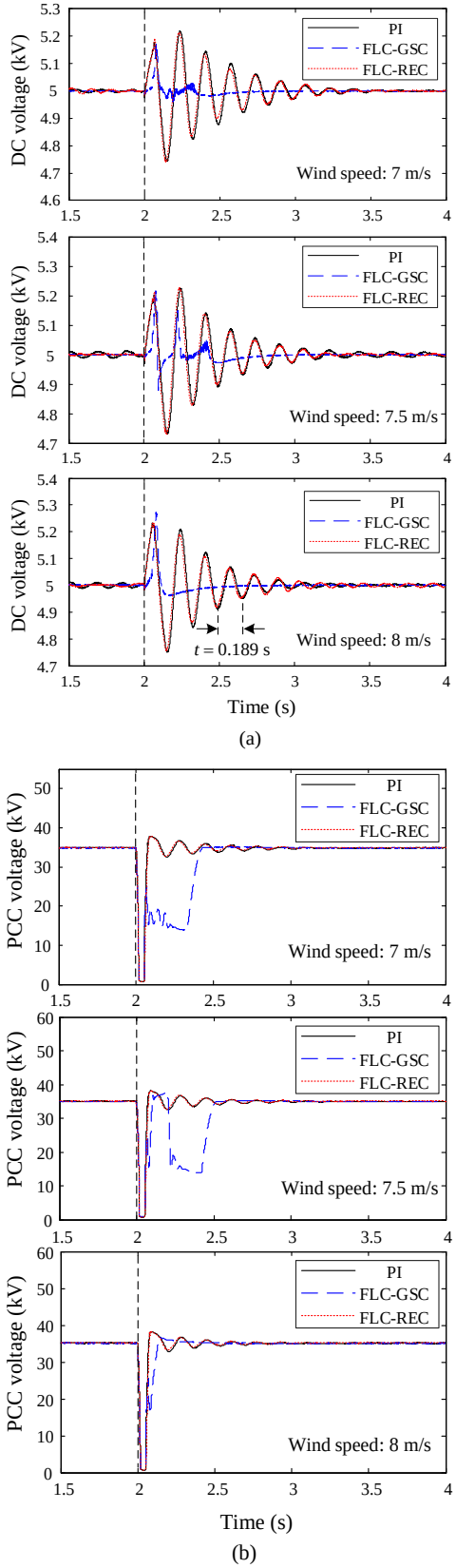

Fig. 12. System dynamics for a three-phase short-circuit ground fault at different wind speeds: (a) DC voltage and (b) PCC voltage.

A large DC capacitor can reduce the DC voltage fluctuations under unbalanced active power [53], as shown in Fig. 13. Therefore, compared with the PI control, a smaller DC

This article has been accepted for publication in a future issue of this journal, but has not been fully edited. Content may change prior to final publication. Citation information: DOI 10.1109/JESTPE.2020.3025081, IEEE Journal of Emerging and Selected Topics in Power Electronics

TABLE II
QUANTITATIVE COMPARISONS AT DIFFERENT WIND SPEEDS UNDER THE PI, FLC-REC, AND FLC-GSC.

Controllers	Eigenvalues			Overshoots			Settling time (s)		
	7 m/s	7.5 m/s	8 m/s	7 m/s	7.5 m/s	8 m/s	7 m/s	7.5 m/s	8 m/s
PI	-0.4108±j26.5002	-0.4726±j26.5004	-0.5040±j26.5000	5.25%	5.37%	4.09%	1.478	1.587	1.424
FLC-REC	-0.4762±j26.6575	-0.5162±j26.6575	-0.5613±j26.6574	5.25%	5.37%	4.09%	1.478	1.424	1.424
FLC-GSC	-5.1770±j48.9020	-5.1770±j48.9018	-5.1770±j48.9018	3.50%	4.32%	4.12%	0.739	0.976	0.924

capacitor can be used in the FLC-GSC to maintain the DC voltage at the same level, which is cost-effective. Meanwhile, it can be seen from Fig. 12(b) that the transient responses of the PCC voltage under the FLC-GSC are faster, but there are large fluctuations in the transient process. This is mainly because the FLC is a model-based control strategy and is sensitive to external disturbances. According to Figs. 10 and 12(a), the quantitative comparisons of the SSO mitigation performances under different wind speeds are shown in Table II, where the eigenvalues, overshoots and settling time of wind farm DC voltage are presented.

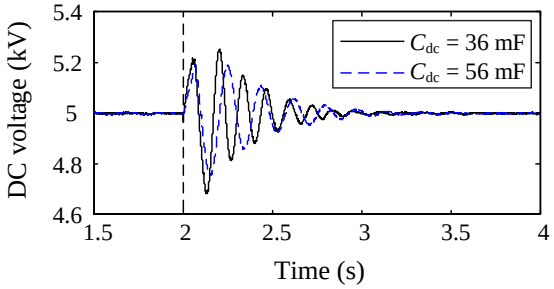

Fig. 13. DC voltage transient responses for three-phase short-circuit ground fault at 2 s with different DC capacitors under the PI control.

2) Different DC Voltages: Under the condition of 8 m/s wind speed, the root locus of the SSO mode under different wind farm DC voltages is shown in Fig. 14 (every two adjacent points have a voltage difference of 0.5 kV).

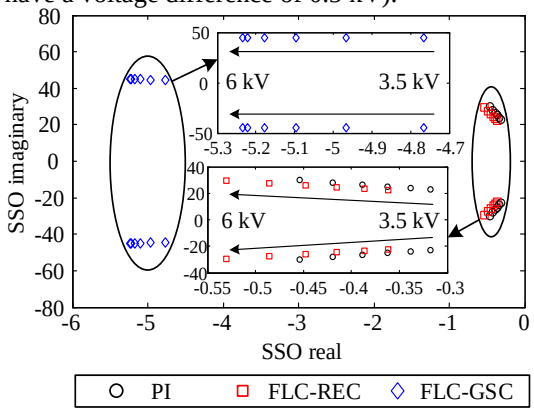

Fig. 14. Root locus of the SSO mode under different wind farm DC voltages.

Fig. 14 shows that compared with the SSO modes under the PI control, the SSO modes under the FLC-GSC are farther from the imaginary axis on the left side of the complex plane, and thus the SSO damping increases under the FLC-GSC. However, there is not much difference between the SSO modes under the FLC-REC and those under the PI control. To verify the theoretical analysis in Fig. 14, PSCAD/EMTDC simulations are performed under different wind farm DC voltages. The disturbance that occurred in the simulations was the same as that in Fig. 12. The responses of the wind farm DC voltage and PCC voltage are shown in Fig. 15.

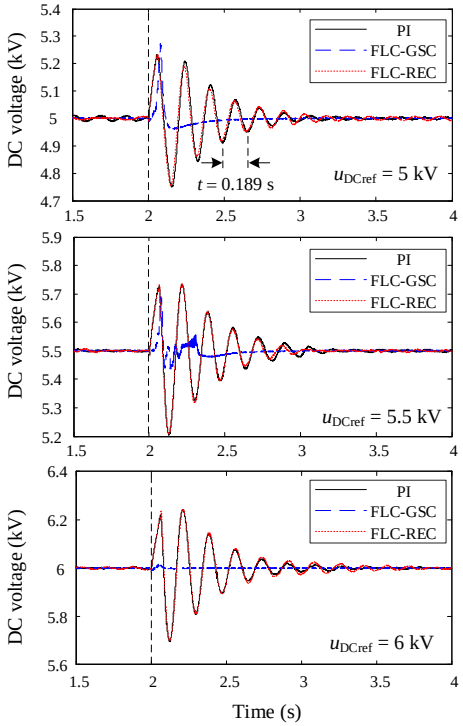

(a)

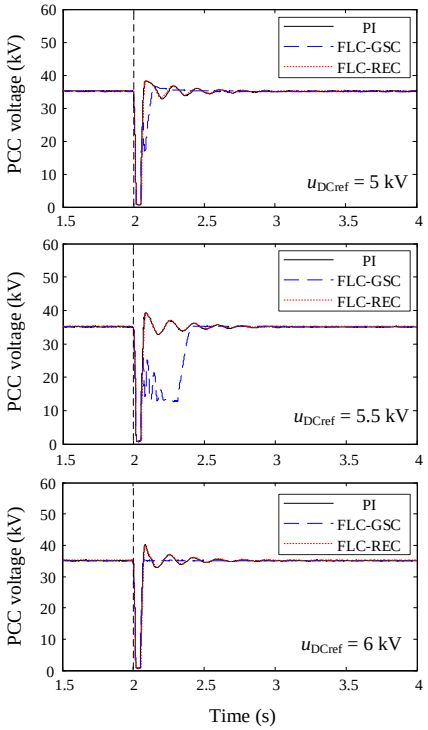

(b)

Fig. 15. System dynamics for a three-phase short-circuit ground fault at different wind farm DC voltages: (a) wind farm DC voltage and (b) PCC voltage.

This article has been accepted for publication in a future issue of this journal, but has not been fully edited. Content may change prior to final publication. Citation information: DOI 10.1109/JESTPE.2020.3025081, IEEE Journal of Emerging and Selected Topics in Power Electronics

TABLE III
QUANTITATIVE COMPARISONS AT DIFFERENT WIND FARM DC VOLTAGES UNDER THE PI, FLC-REC, AND FLC-GSC.

Controllers	Eigenvalues			Overshoots			Settling time (s)		
	5 kV	5.5 kV	6 kV	5 kV	5.5 kV	6 kV	5 kV	5.5 kV	6 kV
PI	-0.3887±j26.5017	-0.4194±j28.1157	-0.4522±j30.0658	4.94%	5.35%	5.00%	1.419	1.269	1.763
FLC-REC	-0.4478±j25.8347	-0.4859±j27.4088	-0.5301±j32.3107	4.94%	5.35%	5.00%	1.419	1.140	1.763
FLC-GSC	-5.1770±j45.0260	-5.2211±j45.0148	-5.2350±j44.9020	5.41%	3.43%	0.44%	0.935	0.960	0.215

It can be seen from Fig. 15 that compared with the PI control and FLC-REC, the SSO damping of the wind farm DC voltage increases significantly under the FLC-GSC, but the fluctuations of the PCC voltage are large when the wind farm DC voltage is 5.5 kV. Meanwhile, the responses of the wind farm DC voltage and PCC voltage under the FLC-REC and PI control are almost identical. This implies that the FLC-REC cannot achieve obvious SSO damping performances. As it can be known from Figs. 14 and 15(a), the quantitative comparisons of the SSO mitigation performances under different wind farm DC voltages are shown in Table III.

3) Different Sizes: To evaluate the SSO mitigation characteristics under different capacity of the wind farm, a wind park including one cluster, two clusters and three clusters is respectively used for the SSO analysis, as shown in Fig. 16. In each cluster, 40 PMSGs with the power rating of 5 MW for each are lumped into one unit of 200 MW capacity. The clusters are linked to the PCC via collector cables, where R_g, L_g and C_g are collector cable parameters with the subscripts "1", "2", and "3", representing the corresponding cluster. The simulation parameters of each cluster are shown in Appendix A, and the wind speed is set to 7 m/s.

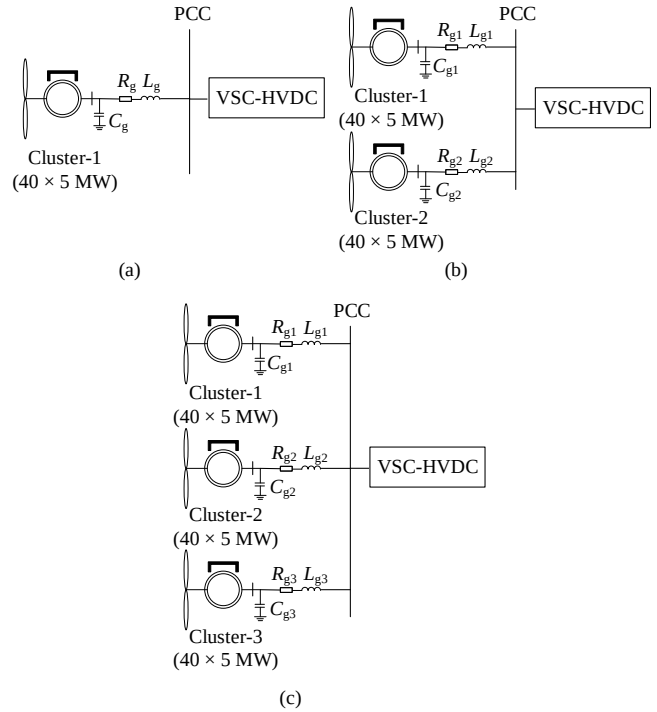

Fig. 16. Wind farms of different sizes: (a) one cluster, (b) two clusters and (c) three clusters.

As the FLC-REC cannot achieve obvious SSO damping, its characteristics are not evaluated. The FLC and PI control are respectively applied in the GSC of each cluster. The disturbance that occurred in the simulation was the same as that in Fig. 12. The responses of the wind farm DC voltage under the PI control and FLC-GSC are shown in Fig. 17.

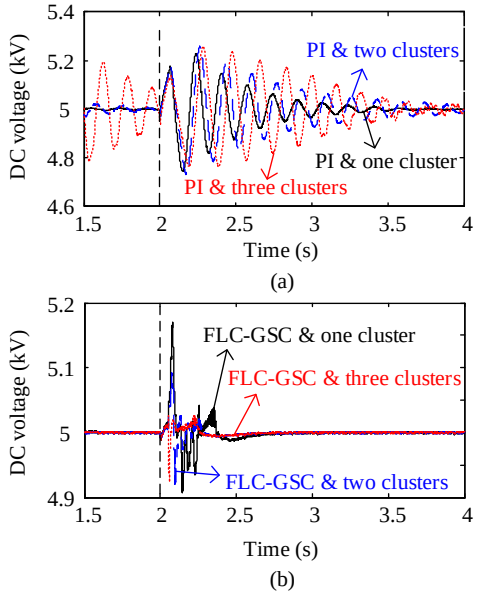

Fig. 17. Wind farm DC voltage dynamics for a three-phase short-circuit ground fault under different sizes of the wind farm: (a) the DC voltage with the PI control and (b) the DC voltage with the FLC-GSC.

It can be seen from Fig. 17(a) that with the increase of the clusters (the capacity) under the PI control, the SSO becomes more serious. This conclusion was also verified in [6], [7], [11] by the eigenvalue and impedance analysis methods. When there are three clusters in the wind farm with the PI control, the DDWFV cannot recover to the stable state within 2 s. In contrast, Fig. 17(b) shows that the FLC-GSC stabilizes the oscillation within 0.76 s under different sizes of the wind farm. With the increase of the clusters (the capacity), the number of the GSCs increases, and then, the nonlinear parts of the GSCs increase, which affects the performance of the DDWFV with the PI control. However, as the FLC-GSC linearizes the GSCs, its performance is less affected by the nonlinear parts. Thus, it can be seen from Fig. 17(b) that the FLC-GSC is less affected by the size of the wind farm. The quantitative comparisons of the overshoots and settling time under different sizes of the wind farm are listed in Table IV, where one, two, and three denote one cluster, two clusters, and three clusters, respectively. It is observed in Table IV that the overshoots and settling time under the FLC-GSC are smaller than those under the PI control. With the increase of the clusters, the settling time of the system with the PI control increases, whereas the settling time is almost unchanged with the FLC-GSC.

TABLE IV
QUANTITATIVE COMPARISONS AT DIFFERENT SIZES OF THE WIND FARM WITH THE PI CONTROL AND FLC-GSC.

Controllers	Overshoots			Settling time (s)		
	One	Two	Three	One	Two	Three
PI	5.14%	5.34%	5.12%	1.373	2	>2
FLC-GSC	3.38%	1.86%	1.52%	0.754	0.737	0.749

This article has been accepted for publication in a future issue of this journal, but has not been fully edited. Content may change prior to final publication. Citation information: DOI 10.1109/JESTPE.2020.3025081, IEEE Journal of Emerging and Selected Topics in Power Electronics

B. *Evaluation of Step Response Characteristics*

The system structure in this case is shown in Fig. 1, and the parameters are shown in Appendix A (the wind speed is set to 8 m/s). The stable operating point of the GSC is operated as u_{DC} = 5 kV and i_{gq} = 0 kA. At t = 2 s, u_{DC} is changed from 5 kV to 6 kV while i_{gq} keeps constant. Fig. 18 illustrates the responses of the PI control and FLC-GSC to a step change in the DC voltage of the wind farm.

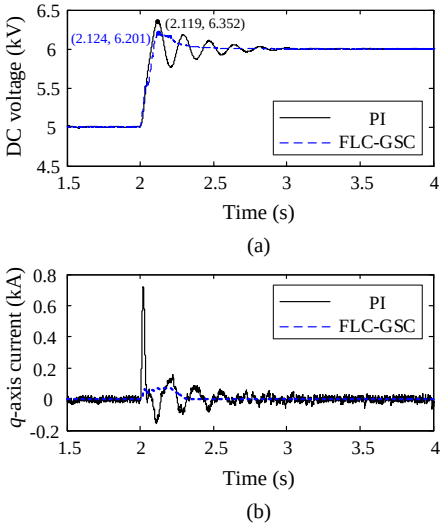

Fig. 18. Performance comparison of the controllers for a step change in the wind farm DC voltage at 2 s.

It can be seen from Fig. 18 that for the PI control, the settling time of u_{DC} is 1.021 s and the overshoot is (6.352 - 6)/6 = 5.87%. For the FLC-GSC, the settling time of u_{DC} is 0.682 s, and the overshoot is (6.201 - 6)/6 = 3.35%. Therefore, both the settling time and overshoot under the FLC-GSC are less than those under the PI control. In addition, an obvious fluctuation appears in i_{gq} under the PI control, whereas the fluctuation under the FLC-GSC is nearly suppressed to zero. This implies that the FLC-GSC achieves a nearly complete decoupling control between each control objective. Similar conclusions can be drawn when i_{gq} is changed from 0 kA to 1 kA at 2 s, as shown in Fig. 19. The better decoupling of the wind farm DC voltage and q-axis current is due to that the FLC realizes the linearization of the control input and output variables of the nonlinear system, thereby realizing the decoupling control between the control input and output variables [42].

C. *Evaluation of Robustness*

In this section, the robustness of the FLC and FLSMC is evaluated through PSCAD/EMTDC simulations under the conditions of parameter uncertainties and external disturbances. The FLC and FLSMC are applied in the GSC, respectively. The wind speed is set to 7 m/s.

1) Parameter Uncertainty: It can be known from (16) and (25) that the values of the DC capacitor (C) and filter inductance (L_g) are included in the control laws of the FLC-GSC and FLSMC. Due to measurement errors, the values of C and L_g may deviate from the actual values. This implies that the measured values of C and L_g in the controllers are uncertain. To evaluate the robust performance of the FLSMC subject to parametric uncertainties, the values of C and L_g in the controllers are set to 50% and 100% of the actual values, respectively. The disturbance that occurred in the simulation was the same as that in Fig. 12. The system transient responses under the FLC-GSC and FLSMC are shown in Figs. 20 and 21.

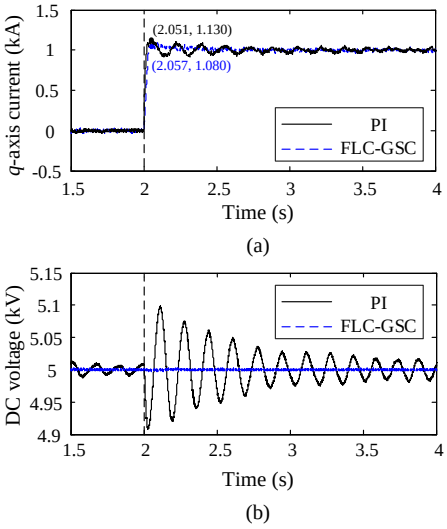

Fig. 19. Performance comparison of the controllers for a step change in the q-axis current of the wind farm at 2 s.

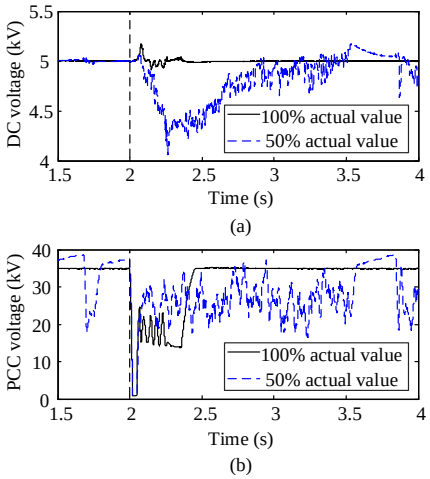

Fig. 20. System transient responses of the FLC-GSC when the measured C and L_g in the controllers are set to 50% and 100% of the actual values: (a) DC voltage and (b) PCC voltage.

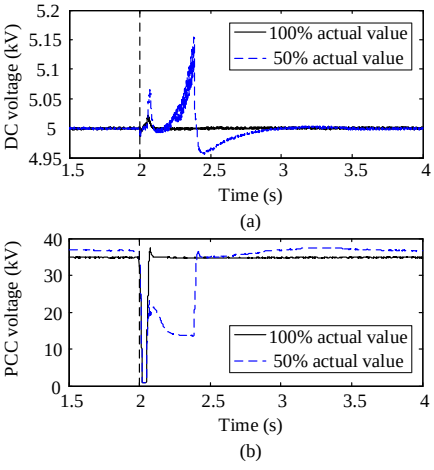

Fig. 21. System transient responses of the FLSMC when the measured C and L_g in the controllers are set to 50% and 100% of the actual values: (a) DC voltage and (b) PCC voltage.

This article has been accepted for publication in a future issue of this journal, but has not been fully edited. Content may change prior to final publication. Citation information: DOI 10.1109/JESTPE.2020.3025081, IEEE Journal of Emerging and Selected Topics in Power Electronics

TABLE V
QUANTITATIVE COMPARISONS OF THE ROBUSTNESS UNDER PARAMETER UNCERTAINTIES AND EXTERNAL DISTURBANCES.

Controllers	Parameter uncertainty				Short-circuit ground fault	
	Overshoot (actual value)	Overshoot (50% actual value)	Settling time/s (actual value)	Settling time/s (50% actual value)	Overshoot	Settling time/s
FLC-GSC	3.71%	Unstable	0.52	Unstable	3.25%	0.866
FLSMC	0.38%	3%	0.155	1.134	0.42%	0.206

As illustrated in Figs. 20 and 21, the wind farm DC voltage and PCC voltage under the FLC-GSC become unstable due to the parameter uncertainties in C and L_g. However, the variables under the FLSMC still remain stable when the measured values in the controllers are set to 50% of the actual values, though with slower response speed and higher overshoots compared with the normal operating condition.

2) Short Circuit Fault: The disturbance that occurred in the simulation was the same as that in Fig. 12. Under 7 m/s wind speed, the responses of the wind farm DC voltage and PCC voltage under the FLC-GSC and FLSMC are shown in Fig. 22.

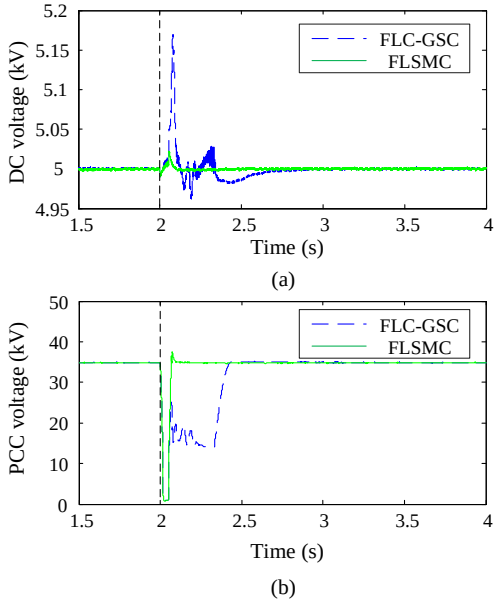

Fig. 22. System transient responses of FLC-GSC and FLSMC for three-phase short-circuit ground fault at 2 s: (a) DC voltage and (b) PCC voltage.

It can be seen from Fig. 22 that compared with the FLC-GSC, the transient fluctuation under the FLSMC is smaller, and then the impact of transient fluctuations on the system is slight. Thus, the FLSMC presents stronger robustness against external disturbances than the FLC-GSC. According to the wind farm DC voltages of Figs. 20-22, the quantitative comparisons of the robustness under the conditions of parameter uncertainties and external disturbances are summarized in Table V.

D. Comparison with SSDC Method

To show that the FLSMC is superior to traditional SSDC methods, the performances of the FLSMC are compared with the SSDC in [16]. The SSDC is composed of a bandpass filter, a compensator, and a limiter, which is shown in Fig. 23. It can be seen from Fig. 23 that locally available variable u_{DC} is used as input signal since it has a great influence on the SSO mode (see Fig. 11). The output signal of SSDC (i_{SSDC}) is added to the inner loop of DC voltage control. The bandpass filter is used to pick out the concerned sub-synchronous signal and avoid interference with the normal control function of GSC. The compensator flexibly adjusts the magnitude and phase of the input signal to achieve better control performance, and it is composed of phase shifters and a gain, as shown in (33).

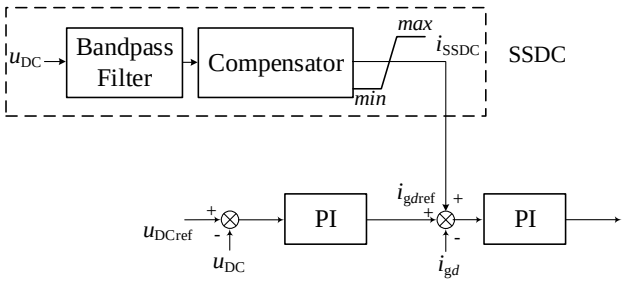

Fig. 23. Structure of the SSDC.

$$T(s) = G\left(\frac{sT_{11}+1}{sT_{12}+1}\right)^m \left(\frac{sT_{21}+1}{sT_{22}+1}\right)^n \tag{33}$$

Based on the parameters in Appendix D, the FLSMC and SSDC are applied in the GSC, respectively. The disturbance that occurred in the simulation was the same as that in Fig. 12. Under the condition of 7 m/s wind speed, the responses of the wind farm DC voltage and PCC voltage under the PI, SSDC, and FLSMC are shown in Fig. 24.

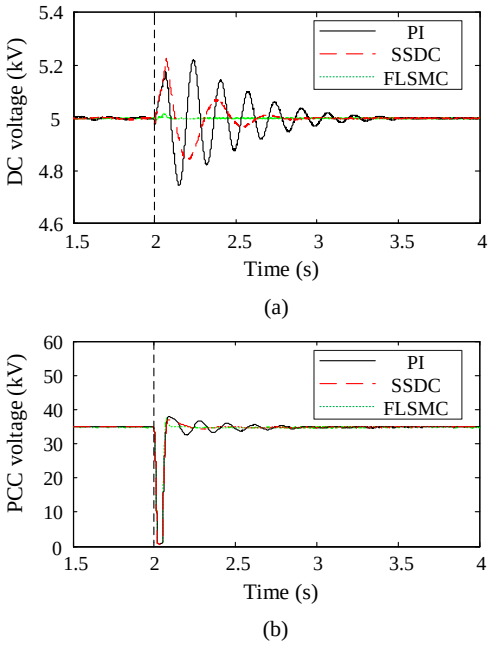

Fig. 24. System transient responses of PI, FLSMC, and SSDC for three-phase short-circuit ground fault at 2 s: (a) DC voltage and (b) PCC voltage.

It can be seen from Fig. 24 that the FLSMC and SSDC both improve the SSO compared with the PI, but the FLSMC shows better SSO mitigation performance and robustness over the SSDC. The main reason is that the FLSMC eliminates the nonlinearities of the GSC and REC, thus presenting better large-signal stability. Meanwhile, the SMC improves the robustness of the DDWFV.

This article has been accepted for publication in a future issue of this journal, but has not been fully edited. Content may change prior to final publication. Citation information: DOI 10.1109/JESTPE.2020.3025081, IEEE Journal of Emerging and Selected Topics in Power Electronics

VII. Conclusion

In this paper, the feedback linearization theory is applied to mitigate the SSO of the DDWFV. The GSC of the wind farm and REC of the VSC-HVDC are partially linearized. Additionally, the SMC is combined with the feedback linearization theory to improve the robustness, and the stability and robustness of the FLSMC are theoretically verified. Finally, the effectiveness and superiority of the FLSMC are verified by an eigenvalue analysis and time-domain simulations. The main conclusions drawn from this paper are summarized as:

1) Compared with the PI control, the FLC eliminates the nonlinearities of the GSC and REC, thus presenting better SSO mitigation performances under various operating conditions. Although the FLC increases the algebraic computation, certain *d*- and *q*-axis PI control loops are cancelled, thus reducing the difficulty of PI parameters tuning.
2) When comparing with the PI control, the FLC exhibits better decoupling control characteristics due to that the FLC can realize the linearization of the control input and output variables of the nonlinear system, thereby realizing the decoupling control between the control input and output variables.
3) In contrast to applying the FLC in the REC, using the FLC in the GSC shows better SSO mitigation characteristics under various operating conditions.
4) Compared with the FLC and SSDC, the FLSMC shows stronger robustness against parameter uncertainties and external disturbances, which reduces the settling time and overshoots of wind farm DC voltage and PCC voltage. Then, a smaller and cheaper DC capacitor can be used in the FLSMC to maintain the DC voltage level.

Appendix A

TABLE A1
Parameters of Equivalent Direct-drive Wind Farm

Modules	Parameters	Value
Wind turbine	Rated power (MW)	40 × 5
	Rated voltage (kV)	3
	Wind speed (m/s)	6
	Wind wheel radius (m)	58
	Air density (kg/m^3)	1.225
	Reference frequency (Hz)	10
	Rotor flux (Wb)	0.0417
	Number of pole pairs	49
	Stator equivalent inductance (H)	0.0121
	DC capacitor C (mF)	56
Collector lines	Filter inductor L_g (H)	0.002
	Resistance R_1 (Ω)	0.05
	Inductor L_1 (H)	0.001
	Capacitor C_1 (μF)	2
	Turn ratio k :1 (kV/kV)	3: 35
	Turn ratio k_2 :1 (kV/kV)	35: 110

TABLE A2
Parameters of VSC-HVDC

Modules	Parameters	Value
AC-side	Filter capacitor C_f (μF)	5
	Equivalent resistance of phase reactor R_c (Ω)	1
	Equivalent inductance of phase reactor L_c (H)	0.015
DC-side	Resistance R_{dc} (Ω)	0.006
	Inductance L_{dc} (H)	0.0005
	Capacitor C_{dc} (μF)	150
	Equivalent DC voltage source u_{dc} (kV)	160

Appendix B

$$\begin{cases} \boldsymbol{f}_{\mathrm{w}}(\boldsymbol{x}) = \begin{bmatrix} \dfrac{i_{\mathrm{dc1}}}{C} \\ -\dfrac{1}{L_{\mathrm{g}}}u_{gd} + \omega_{\mathrm{g}} i_{gq} \\ -\dfrac{1}{L_{\mathrm{g}}}u_{gq} - \omega_{\mathrm{g}} i_{gd} \end{bmatrix}, \ \boldsymbol{g}_{\mathrm{w}}(\boldsymbol{x}) = \begin{bmatrix} -\dfrac{3i_{gd}}{2Cu_{\mathrm{DC}}} & -\dfrac{3i_{gq}}{2Cu_{\mathrm{DC}}} \\ \dfrac{1}{L_{\mathrm{g}}} & 0 \\ 0 & \dfrac{1}{L_{\mathrm{g}}} \end{bmatrix} \end{cases} \tag{B1}$$

$$\begin{cases} \boldsymbol{f}_{\mathrm{v}}(\boldsymbol{x}) = \begin{bmatrix} \dfrac{1}{C_{\mathrm{f}}}i_{2d} - \dfrac{1}{C_{\mathrm{f}}}i_{sd} + \omega_{\mathrm{g}} u_{sq} \\ \dfrac{1}{C_{\mathrm{f}}}i_{2q} - \dfrac{1}{C_{\mathrm{f}}}i_{sq} - \omega_{\mathrm{g}} u_{sd} \\ \dfrac{1}{L_{\mathrm{c}}}u_{sd} - \dfrac{R_{\mathrm{c}}}{L_{\mathrm{c}}}i_{sd} + \omega_{\mathrm{g}} i_{sq} \\ \dfrac{1}{L_{\mathrm{c}}}u_{sq} - \dfrac{R_{\mathrm{c}}}{L_{\mathrm{c}}}i_{sq} - \omega_{\mathrm{g}} i_{sd} \\ -\dfrac{i_{\mathrm{dc}}}{C_{\mathrm{dc}}} \end{bmatrix}, \ \boldsymbol{g}_{\mathrm{v}}(\boldsymbol{x}) = \begin{pmatrix} 0 & 0 \\ 0 & 0 \\ -\dfrac{1}{L_{\mathrm{c}}} & 0 \\ 0 & -\dfrac{1}{L_{\mathrm{c}}} \\ \dfrac{3i_{sd}}{2C_{\mathrm{dc}}u_{\mathrm{dc1}}} & \dfrac{3i_{sq}}{2C_{\mathrm{dc}}u_{\mathrm{dc1}}} \end{pmatrix} \end{cases} \tag{B2}$$

Appendix C

To examine the internal dynamics stability of the GSC and REC, the coordinate transformation needs to be constructed for $\boldsymbol{z}_{\mathrm{wi}}$ and $\boldsymbol{z}_{\mathrm{vi}}$ to satisfy 1) the Jacobian matrix is nonsingular, and 2) the following assumption holds:

$$\lim_{t\to\infty} h_{\mathrm{i}}(x) \to 0 \tag{C1}$$

(C1) indicates that the system dynamics approach zero when time approaches infinity. To satisfy the above conditions, we select $\boldsymbol{z}_{\mathrm{wi}}$ as

$$\boldsymbol{z}_{\mathrm{wi}} = \left[-\frac{1}{2}L_{\mathrm{g}}i_{gd}^2 - \frac{1}{2}L_{\mathrm{g}}i_{gq}^2 - \frac{1}{2}Cu_{\mathrm{DC}}^2 \right] \tag{C2}$$

Under the condition of (C1), for the GSC of wind farm, $h_{\mathrm{w1}}(x) = z_{\mathrm{wo1}} = u_{\mathrm{DC}} = 0$ and $h_{\mathrm{w2}}(x) = z_{\mathrm{wo2}} = i_{gq} = 0$. Therefore, (C2) is simplified as

$$\boldsymbol{z}_{\mathrm{wi}} = \left[-\frac{1}{2}L_{\mathrm{g}}i_{gd}^2 \right] \tag{C3}$$

The dynamic equation of $\boldsymbol{z}_{\mathrm{wi}}$ is obtained from (1) as

$$\dot{\boldsymbol{z}}_{\mathrm{wi}} = \left[i_{gd}(u_{gd} - u_{wd}) \right] \tag{C4}$$

Since $u_{gd} < u_{\mathrm{wd}}$, $\mathrm{d}\boldsymbol{z}_{\mathrm{wi}}/\mathrm{d}t < 0$. Thus, (C4) is the internal dynamic equation of the GSC representing a stable system. Similarly, for the REC, $\boldsymbol{z}_{\mathrm{vi}}$ is selected as

$$\boldsymbol{z}_{\mathrm{vi}} = \left[-\frac{1}{2}C_{\mathrm{f}}u_{sd}^2 - \frac{1}{2}C_{\mathrm{f}}u_{sq}^2 - \frac{1}{2}C_{\mathrm{dc}}u_{\mathrm{dc1}}^2 \right] \tag{C5}$$

Under the condition of (C1), $h_{\mathrm{v1}}(x) = z_{\mathrm{vo1}} = u_{sd} = 0$ and $h_{\mathrm{v2}}(x) = z_{\mathrm{vo2}} = u_{sq} = 0$, and then (C5) is simplified as

$$\boldsymbol{z}_{\mathrm{vi}} = \left[-\frac{1}{2}C_{\mathrm{dc}}u_{\mathrm{dc1}}^2 \right] \tag{C6}$$

The dynamic equation of $\boldsymbol{z}_{\mathrm{vi}}$ is obtained from (2) as

$$\dot{\boldsymbol{z}}_{\mathrm{vi}} = \left[u_{\mathrm{dc1}}i_{\mathrm{dc}} - \frac{3}{2}\left(u_{\mathrm{vd}}i_{sd} + u_{\mathrm{vq}}i_{sq}\right) \right] \tag{C7}$$

According to Fig. 1, the following relationship holds when the system is in steady-state operation condition:

$$\begin{cases} \dfrac{3}{2}(u_{vd}i_{sd}+u_{vq}i_{sq}) = u_{dc1}i_{dc3}+\dfrac{P_0}{C_{dc}u_{dc1}} \\ i_{dc3}=i_{dc} \end{cases} \tag{C8}$$

It can be known form (C8) that

$$u_{dc1}i_{dc} < \frac{3}{2}\left(u_{vd}i_{sd}+u_{vq}i_{sq}\right) \tag{C9}$$

Thus, it can be known from (C7) that $d\mathbf{z}_{vi}/dt < 0$, which implies that the internal dynamic of the REC is stable. As the internal dynamics of the GSC and REC are both stable, the PFL method is implementable to the GSC and REC of the DDWFV.

APPENDIX D

TABLE D1
REFERENCE VALUES OF CONTROL SYSTEMS

Modules	Parameters	Value
MSC	d-axis current reference i_{sdref} (kA)	0
	Speed reference ω_{sref} (rad/s)	37.699
GSC	DC voltage reference u_{DCref} (kV)	5
	q-axis current reference i_{gqref} (kA)	0
REC	d-axis voltage reference u_{sdref} (kV)	89.815
	q-axis voltage reference u_{sqref} (kV)	0

TABLE D2
PARAMETERS OF PI CONTROLLERS

Modules	Parameters	Value
MSC	Unity power factor control coefficient (proportional k_{p1}, integral k_{i1})	1, 5
	Speed control outer loop coefficient (proportional k_{p2}, integral k_{i2})	0.4, 2.5
	Speed control inner loop coefficient (proportional k_{p3}, integral k_{i3})	1, 5
GSC	DC voltage control outer loop coefficient (proportional k_{p4}, integral k_{i4})	0.2, 133
	DC voltage control inner loop coefficient (proportional k_{p5}, integral k_{i5})	0.6, 2.5
	q-axis current control coefficient (proportional k_{p6}, integral k_{i6})	0.6, 2.5
PLL	Proportional k_{p_pll}, integral k_{i_pll}	5, 9
REC	d-axis voltage control outer loop coefficient (proportional k_{p9}, integral k_{i9})	0.0029, 100
	q-axis voltage control outer loop coefficient (proportional k_{p10}, integral k_{i10})	0.0029, 100
	d-axis voltage control inner loop coefficient (proportional k_{p7}, integral k_{i7})	2.5, 10000
	q-axis voltage control inner loop coefficient (proportional k_{p8}, integral k_{i8})	2.5, 10000

TABLE D3
PARAMETERS OF FLC

Parameters	Value
k_{wp1}, k_{wi1}	350, 2000
k_{wp2}, k_{wi2}	350, 2000
k_{vp1}, k_{vi1}	75, 111
k_{vp2}, k_{vi2}	60, 1111

TABLE D4
PARAMETERS OF FLSMC

Parameters	Value
ε_{wd}, ε_{wq}	100, 100
ε_{vd}, ε_{vq}	100, 100

TABLE D5
PARAMETERS OF SSDC

Modules	Parameters	Value
4-order Butterworth bandpass filter	Center frequency (Hz)	5.3
	Bandwidth (Hz)	2
Compensator	G	3
	T_{11}	2.4
	T_{12}	0.4
	T_{21}	1.6
	T_{22}	2.1
	m	1
	n	1
Limiter	Amplitude (p.u.)	0.1

REFERENCES

[1] Global Wind Energy Council (GWEC), "Global Wind Report 2019," Brussels, Belgium, Mar. 2020.

[2] F. Blaabjerg and K. Ma, "Wind energy systems," *Proc. IEEE*, vol. 105, no. 11, pp. 2116-2131, Nov. 2017.

[3] R. Basak, G. Bhuvaneswari, and R. R. Pillai, "Low-voltage-ride-through of a synchronous generator-based variable speed grid-interfaced wind energy conversion system," *IEEE Trans. Ind. Appl.*, vol. 56, no. 1, pp. 752-762, Jan.-Feb. 2020.

[4] A. Korompili, Q. Wu, and H. Zhao, "Review of VSC HVDC conenction for offshore wind power integration," *Renew. Sust. Energ. Rev.*, vol. 59, pp. 1405-1414, Jun. 2016.

[5] M. Amin and M. Molinas, "Understanding the origin of oscillatory phenomena observed between wind farms and HVdc systems," *IEEE J. Emerg. Sel. Top. Power Electron.*, vol. 5, no. 1, pp. 378-392, Mar. 2017.

[6] J. Lyu, X. Cai, M. Amin, and M. Molinas, "Sub-synchronous oscillation mechanism and its suppression in MMC-based HVDC connected wind farms," *IET Gener. Trans. Distr.*, vol. 32, no. 2, pp. 458-470, Feb. 2017.

[7] H. Liu and J. Sun, "Voltage stability and control of offshore wind farms with AC collection and HVDC transmission," *IEEE J. Emerg. Sel. Top. Power Electron.*, vol. 2, no. 4, pp. 1181-1189, Dec. 2014.

[8] K. Sun, W. Yao, J. Fang, X. Ai, J. Wen, and S. Cheng, "Impedance modeling and stability analysis of grid-connected DFIG-based wind farm with a VSC-HVDC," *IEEE J. Emerg. Sel. Top. Power Electron.*, vol. 8, no. 2, pp. 1375-1390, Jun. 2020.

[9] S. Zhao and B. Shao, "An analytical method suitable for revealing the instability mechanism of power electronics dominated power systems," *Int. J. Electr. Power Energy Syst.*, vol. 109, pp. 269-282, Jul. 2019.

[10] L. P. Kunjumuhammed, B. C. Pal, R. Gupta, and K. J. Dyke, "Stability analysis of a PMSG-based large offshore wind farm connected to a VSC-HVDC," *IEEE Trans. Energy Convers.*, vol. 32, no. 3, pp. 1166-1176, Sept. 2017.

[11] Y. Wang, C. Zhao, C. Guo, and A. U. Rehman, "Dynamics and small signal stability analysis of PMSG-based wind farm with an MMC-HVDC system," *CSEE J. Power Energy Syst.*, vol. 6, no. 1, pp. 226-235, Mar. 2020.

[12] W. Du, Q. Fu, and H. Wang, "Subsynchronous oscillations caused by open-loop modal coupling between VSC-based HVDC line and power system," *IEEE Trans. Power Syst.*, vol. 33, no. 4, pp. 3664-3677, Jul. 2018.

[13] J. Adams, V. A. Pappu, and A. Dixit, "Ercot experience screening for sub-synchronous control interaction in the vicinity of series capacitor banks," in *Proc. Power Energy Soc. Gen. Mee.*, San Diego, CA, 2012, pp. 1-5.

[14] M. Sahni, B. Badrzadeh, D. Muthumuni, Y. Cheng, H. Yin, S. H. Huang, and Y. Zhou, "Sub-synchronous interaction in wind power plants – part II: an ERCOT case study," in *Proc. Power Energy Soc. Gen. Mee.*, San Diego, CA, 2012, pp. 1-9.

[15] X. Xie, X. Zhang, H. Liu, H. Liu, Y. Li, and C. Zhang, "Characteristic analysis of subsynchronous resonance in practical wind farms connected to series-compensated transmissions," *IEEE Trans. Energy Convers.*, vol. 32, no. 3, pp. 1117-1126, Sept. 2017.

[16] H. Liu, X. Xie, J. He, T. Xu, Z. Yu, C. Wang, and C. Zhang, "Subsynchronous interaction between direct-drive PMSG based wind farms and weak AC networks," *IEEE Trans. Power Syst.*, vol. 32, no. 6, pp. 4708-4720, Nov. 2017.

[17] J. Shair, X. Xie, L. Wang, W. Liu, J. He, and H. Liu, "Overview of emerging subsynchronous oscillations in practical wind power systems," *Renew. Sust. Energ. Rev.*, vol. 99, pp. 159-168, Jan. 2019.

[18] Y. Song and F. Blaabjerg, "Overview of DFIG-based wind power system resonances under weak networks," *IEEE Trans. Power Electron.*, vol. 32, no. 6, pp. 4370-4394, Jun. 2017.

[19] A. Testa *et al.*, "Interharmonics: theory and modeling," *IEEE Trans. Power Deliv.*, vol. 22, no. 4, pp. 2335-2348, Oct. 2007.

[20] A. Testa and R. Langella, "Power system subharmonics," in *Proc. Power Energy Soc. Gen. Mee.*, San Diego, CA, 2005, pp. 2237-2242.

[21] V. B. Virulkar and G. V. Gotmare, "Sub-synchronous resonance in series compensated wind farm: a review," *Renew. Sust. Energ. Rev.*, vol. 55, pp. 1010-1029, Mar. 2016.

[22] M. S. El-Moursi, B. Bak-Jensen, and M. H. Abdel-Rahman, "Novel STATCOM controller for mitigating SSR and damping power system oscillations in a series compensated wind park," *IEEE Trans. Power Electron.*, vol. 25, no. 2, pp. 429-441, Feb. 2010.

[23] H. A. Mohammadpour, M. M. lslam, E. Santi, and Y. Shin, "SSR damping in fixed-speed wind farms using series FACTS controllers," *IEEE Trans. Power Deliv.*, vol. 31, no. 1, pp. 76-86, Feb. 2016.

[24] H. A. Mohammadpour and E. Santi, "Modeling and control of gate-controlled series capacitor interfaced with a DFIG-based wind farm," *IEEE Trans. Ind. Electron.*, vol. 62, no. 2, pp. 1022-1033, Feb. 2015.

[25] X. Zhang, X. Xie, J. Shair, H. Liu, Y. Li, and Y. Li, "A grid-side subsynchronous damping controller to mitigate unstable SSCI and its hardware-in-the-loop tests," *IEEE Trans. Sustain. Energy*, vol. 11, no. 3, pp. 1548-1558, Jul. 2020.

[26] S. Golshannavaz, F. Aminifar, and D. Nazarpour, "Application of UPFC to enhancing oscillatory response of series-compensated wind farm integrations," *IEEE Trans. Smart Grid*, vol. 5, no. 4, pp. 1961-1968, Jul. 2014.

[27] X. Bian, Y. Ding, Q. Jia, L. Shi, X. Zhang, and K. L. Lo, "Mitigating of sub-synchronous control interaction of a power system with DFIG-based wind farm under multi-operating points," *IET Gener. Trans. Distr.*, vol. 12, no. 21, pp. 5834-5842, Nov. 2018.

[28] M. Ghafouri, U. Karaagac, H. Karimi, S. Jensen, J. Mahseredjian, and S. O. Faried, "An LQR controller for damping of subsynchronous interaction in DFIG-based wind farms," *IEEE Trans. Power Syst.*, vol. 32, no. 6, pp. 4934-4942, Nov. 2017.

[29] L. Fan and Z. Miao, "Mitigating SSR using DFIG-based wind generation," *IEEE Trans. Sustain. Energy*, vol. 3, no. 3, pp. 349-358, Jul. 2012.

[30] Y. Song and F. Blaabjerg, "Wide frequency band active damping strategy for DFIG system high frequency resonance," *IEEE Trans. Energy Convers.*, vol. 31, no. 4, pp. 1665-1675, Dec. 2016.

[31] J. Lv, P. Dong, G. Shi, X. Cai, H. Rao, and J. Chen, "Subsynchronous oscillation of large DFIG-based wind farms integration through MMC-based HVDC," in *Proc. Int. Conf. on Power Syst. Technol.*, 2014, pp. 2401-2408.

[32] J. Lyu, M. Molinas, and X. Cai, "Stabilization control methods for enhancing the stability of wind farm integration via an MMC-based HVDC system," in *Proc. CPE-POWERENG*, 2017, pp. 324-329.

[33] M. T. Ali, D. Zhou, Y. Song, M. Ghandhari, L. Harnefors, and F. Blaabjerg, "Analysis and mitigation of SSCI in DFIG systems with experimental validation," *IEEE Trans. Energy Convers.*, vol. 35, no. 2, pp. 713-723, Jun. 2020.

[34] J. Lyu, X. Cai, and M. Molinas, "Optimal design of controller parameters for improving the stability of MMC-HVDC for wind farm integration," *IEEE J. Emerg. Sel. Top. Power Electron.*, vol. 6, no. 1, pp. 40-53, Mar. 2018.

[35] M. Ghafouri, U. Karaagac, J. Mahseredjian, and H. Karimi, "SSCI damping controller design for series-compensated DFIG-based wind parks considering implementation challenges," *IEEE Trans. Power Syst.*, vol. 33, no. 4, pp. 3664-3677, Jul. 2018.

[36] A. Chen, D. Xie, D. Zhang, C. Gu, and K. Wang, "PI parameter tuning of converters for sub-synchronous interactions existing in grid-connected DFIG wind turbines," *IEEE Trans. Power Electron.*, vol. 34, no. 7, pp. 6345-6355, Jul. 2019.

[37] A. E. Leon and J. A. Solsona, "Sub-synchronous interaction damping control for DFIG wind turbines," *IEEE Trans. Power Syst.*, vol. 30, no. 1, pp. 419-428, Jan. 2015.

[38] J. Shair, X. Xie, and G. Yan, "Mitigating subsynchronous control interaction in wind power systems: existing techniques and open challenges," *Renew. Sust. Energ. Rev.*, vol. 108, pp. 330-346, Jul. 2019.

[39] A. Isidori, *Nonlinear Control Systems.* Berlin, Germany: Springer-Verlag, 1989.

[40] T. F. Orchi, M. A. Mahmud, and A. M. T. Oo, "Design of feedback linearizing model predictive controllers for grid-connected systems with multiple photovoltaic units," in *Proc. IEEE Int. Conf. on PEDES*, Chennai, India, 2018, pp. 1-6.

[41] K. Kim, Y. Jeung, D. Lee, and H. Kim, "LVRT scheme of PMSG wind power systems based on feedback linearization," *IEEE Trans. Power Electron.*, vol. 27, no. 5, pp. 2376-2384, May 2012.

[42] Z. Li, Q. Hao, F. Gao, L. Wu, and M. Guan, "Nonlinear decoupling control of two-terminal MMC-HVDC based on feedback linearization," *IEEE Trans. Power Deliv.*, vol. 34, no. 1, pp. 376-386, Feb. 2019.

[43] M. A. Mahmud, T. K. Roy, S. Saha, M. E. Haque, and H. R. Pota, "Robust nonlinear adaptive feedback linearizing decentralized controller design for islanded DC microgrids," *IEEE Trans. Ind. Appl.*, vol. 55, no. 5, pp. 5343-5352, Sep.-Oct. 2019.

[44] M. A. Chowdhury and G. M. Shafiullah, "SSR mitigation of series-compensated DFIG wind farms by a nonlinear damping controller using partial feedback linearization," *IEEE Trans. Power Syst.*, vol. 33, no. 3, pp. 2528-2538, May 2018.

[45] M. A. Chowdhury, M. A. Mahmud, W. Shen, and H. R. Pota, "Nonlinear controller design for series-compensated DFIG-based wind farms to mitigate subsynchronous control interaction," *IEEE Trans. Energy Convers.*, vol. 32, no. 2, pp. 707-719, Jun. 2017.

[46] C. Califano, S. Monaco, and D. Normand-Cyrot, "On the problem of feedback linearization," *Systems & Control Letters*, vol. 36, no. 1, pp. 61-67, Jan. 1999.

[47] V. Utkin, *Sliding Modes in Control and Optimization.* New York: Springer-Verlag, 1992.

[48] M. Castilla, L. Vicuna, J. M. Guerrero. J. Matas, and J. Miret, "Sliding-mode control of quantum series-parallel resonant converters via input-output linearization," *IEEE Trans. Ind. Electron.*, vol. 52, no. 2, pp. 566-575, Apr. 2005.

[49] W. Gao and J. C. Hung, "Variable structure control of nonlinear systems: a new approach," *IEEE Trans. Ind. Electron.*, vol. 40, no. 1, pp. 45-55, Feb. 1993.

[50] J. Yao, X. Wang, J. Li, R. Liu, and H. Zhang, "Sub-synchronous resonance damping control for series-compensated DFIG -based wind farm with improved particle swarm optimization," *IEEE Trans. Energy Convers.*, vol. 34, no. 2, pp. 843-859, Jun. 2020.

[51] J. Shair, X. Xie, Y. Li, and V. Terzija, "Hardware-in-the-loop and field validation of a rotor-side subsynchronous damping controller for a DFIG connected to a series compensated line," *IEEE Trans. Power Deliv.*, 2020. (Early access).

[52] X. Xie, Q. Jiang, and Y. Han, "Damping multimodal subsynchronous resonance using a static var compensator controller optimized by genetic algorithm and simulated annealing," *Eur. Trans. Elect. Power*, vol. 22, no. 8, pp. 1191-1204, 2012.

[53] P. Liutanakul, S. Pierfederici, and F. Meibody-Tabar, "Application of SMC with I/O feedback linearization to the control of the cascade controlled-rectifier/inverter-motor drive system with small dc-link capacitor," *IEEE Trans. Power Electron.*, vol. 23, no. 5, pp. 2489-2499, Sept. 2008.